Beam intensities with EURISOL

1. General considerations

It is the purpose of a future European ISOL-based secondary-beam facility to deliver beams of radioactive nuclei with the highest intensities and with the most wide-spread neutron-to-proton ratio possible for experiments, which aim for improving our knowledge on nuclear properties far from the valley of beta stability. Obviously, the estimation of the available secondary-beam intensities and in particular of the limitations in their neutron-to-proton ratio is of prime importance for the prospects of such a facility. Moreover, these estimations, performed for different possible technical solutions, have a decisive influence on the preferences given to the different technical options in the design phase. In the preparation of the second phase of the EURISOL Design Study [1], a specific task group has been established for this purpose. Please note, that the first estimates on the attainable secondary-beam intensities at EURISOL have already been performed during the R&D phase (see the report of the Target-and-Ion-Source group in the EURISOL RTD report, Appendix C [2]).

The actual knowledge on attainable beam intensities in ISOL-based secondary-beam facilities, driven by protons of about 1 GeV, mostly relies on the long-term experience in such facilities, e.g. ISOLDE at CERN. However, it is not easy to disentangle the formation cross sections, which are given by physics, and the release, ionization, and transport efficiencies, which are subject to progress in technology. Systematic data on spallation cross sections with protons around 1 GeV became available only few years ago for selected systems (see e.g. [3]) by innovative inverse-kinematics experiments at GSI-Darmstadt, Germany. At lower energies, nuclide cross sections from nucleon- or heavy-ion induced reactions were at that time still scarce. To overcome these limitations, large experimental efforts have been underdone in partners' institutes. Moreover, studies underdone on the complex scenario of fragmenting post-accelerated ISOL beams as a promising option to access extremely neutron-rich nuclides and on the reactions of heavy-ions have provide key information for technical options of the EURISOL design.

1.1 Nuclear-reaction aspects

The nuclides of interest are produced by the most suitable nuclear reaction using primordial nuclei as projectile and/or target. Therefore, a good understanding of the nuclear reactions involved is of prime importance. In view of many different parameters to be varied, e.g. projectile energy, projectile and target composition, realistic nuclear-reaction models with high predictive power are mandatory. In the same time, these models need to be verified with sufficiently wide-spread and systematic experimental results.

Sketching the extremes, the nuclear reactions can be classified in nucleon (proton or neutron, also deuteron) induced reactions and nucleus-nucleus collisions. Averaged over impact parameter, they typically show different features with increasing bombarding energy. Nucleon-induced reactions evolve from capture or complete fusion over pre-equilibrium phenomena to intra-nuclear cascades. Nucleus-nucleus collisions evolve from complete fusion over deep-inelastic reactions and incomplete fusion to abrasion-like reactions. When fissile nuclei are involved, nuclear fission forms one possible decay branch of the system, which is very complex and whose features drastically vary as a function of excitation energy, angular momentum and nuclear composition.

In the thick-target environment of realistic scenarios, not only the primary production but also the transport phenomena of secondary reaction products and their consecutive reactions in the target play an important role. Therefore, knowledge on reactions induced by protons and, more important, neutrons, over a large energy range is mandatory.

1.2 Aspects of primary-beam preparation

For a specific reaction product with a given production cross section, the production rate relies on the available or usable primary-beam intensity and the usable target thickness. Limitations are given by manifold effects:

- Technical limitations of the primary accelerator impose an upper limit on the available primary-beam intensity.
- The heat load in the target due to electronic interactions of the projectiles gives an upper limit on the usable primary-beam intensity.
- The energy loss of the projectile in the target due to electronic interactions gives an upper limit on the usable target thickness.
- The attenuation of the beam along its path due to all kind of nuclear reactions gives an upper limit on the usable target thickness.

In general, to minimize parasitic effects it is advantageous to use light charged-particle beams with high energies, or as an alternative option, which completely avoids electronic interactions, to use neutrons as projectiles. Double-stage target scenarios for neutron production have, thus, been considered.

Also the aspects of extraction (see below) may induce severe limitations on the heat load in the target or on the geometry of the target assembly, thus limiting the secondary-beam intensities.

1.3 Aspects of extraction, ionization and re-acceleration of secondary nuclides

In an ISOL-based system, it is a complex task to extract the reaction products out of the target and to transform them into a re-accelerated secondary beam. In this process, severe losses may appear. It is an important task to optimise the different steps of this process by developing adequate and innovative technological solutions. They are more or less specific for every element and also vary as a function of lifetime of the nuclide considered. The development of such optimised procedures forms part of other dedicated tasks (see reports of Tasks 3 [4], 4 [5] and 9 [6]).

For the present task, more general estimations on the potential figures of merit of the extraction, ionisation and acceleration of the reaction products are needed.

1.4 Complex scenarios

The limitations of a “standard” ISOL facility, in particular in producing radioactive nuclides with extreme neutron-to-proton ratio might be essentially overcome by using multiple-step reactions in specifically designed complex scenarios. A possible option would consist of producing a neutron-rich secondary beam based on fission in a “standard” ISOL procedure and fragmenting it after acceleration [7]. This option has been studied in details during the EURISOL Design Study phase.

2. Results

2.1. Nuclear-reaction aspects

Different types of nuclear reactions are exploited for the nuclide production in the standard design of the EURISOL project, driven by a 1 GeV proton beam. In the direct-target option, spallation-evaporation and spallation-fission residues are produced in mostly direct interactions of the primary protons with different target material. In the high-power fission-target option, secondary neutrons from a converter target induce fission in a target at excitation energies mostly up to a few MeV above the fission barrier. Additionally to this standard option, heavy-ion collisions in a two-step option [7] represent an interesting opportunity for production of exotic nuclei not reachable with the standard option.

2.1.1 Spallation reactions

Spallation reactions with protons around 1 GeV seem to be a versatile and rather optimum tool for the production of both neutron-deficient and neutron-rich isotopes of all elements up to uranium. The "classical" production mechanism used for the very successful long-time operation of ISOLDE has been the spallation reaction, induced by 600 MeV protons; recently also higher energies became available.

The understanding of this reaction mechanism has tremendously been improved recently by systematic experiments performed in inverse kinematics with the unique installations available at GSI. Innovative experiments in inverse kinematics are the only ones, which give a full identification of A and Z of all reaction products. Thus, this type of measurements, provide an global overview on the potential of spallation reactions for the production of radioactive nuclides and an excellent basis for benchmarking and improving of different theoretical models.

Figure 1 present the measured nuclide distributions for 1 GeV proton-induced reactions on ^{56}Fe, ^{136}Xe, ^{208}Pb and ^{238}U, measured in inverse kinematics [8, 9, 10, 11, 12, 13, 14, 15]. This general overview reveals the following general characteristics of the spallation reaction:

- Spallation-evaporation residues populate neutron-rich isotopes of a few elements below the target[1]) with strongly decreasing cross sections by cold-fragmentation reactions [16].
- The main nuclide production by spallation-evaporation reactions gradually tends towards the proton-rich side and extends to roughly 10 to 15 elements below the target element. Saturation in the production of the most neutron-deficient isotopes is reached around 5 elements below the target, where the cross sections already decrease. Lighter residues are situated closer to the beta-stability line.
- Spallation-fission reactions with actinide targets produce neutron-rich isotopes in a wide element range (extending from $Z = 10$ to $Z = 60$ and further) with high cross sections. On the other hand, spallation-fission reactions with lighter targets (e.g. lead) are not interesting for the production of radioactive beams, because they produce nuclides rather close to the beta-stability line. Moreover, the cross sections are rather low.

These characteristics were already qualitatively known before and were exploited e.g. for the production of radioactive species at the ISOLDE facility. However, the new experimental results and the improved codes provide a better quantitative and systematic knowledge. Moreover, due to the high-precision information on the velocities of final fragments measured at the FRS, it is possible to determine through which reaction mechanism (e.g. fission or evaporation) the observed fragment was formed, see e.g. [14].

As an example of model calculations, in Figure 2 is shown a comparison between the data measured in the 1 GeV proton-induced spallation on ^{238}U [12, 13, 14, 15] and the results of the ABRABLA07 model [14,17,18].

---

[1]) Although the experiment was performed in inverse kinematics, we refer here to normal kinematics, which is applied in the EURISOL scenario. Therefore, the heavy reaction partner is denoted as the target nucleus.

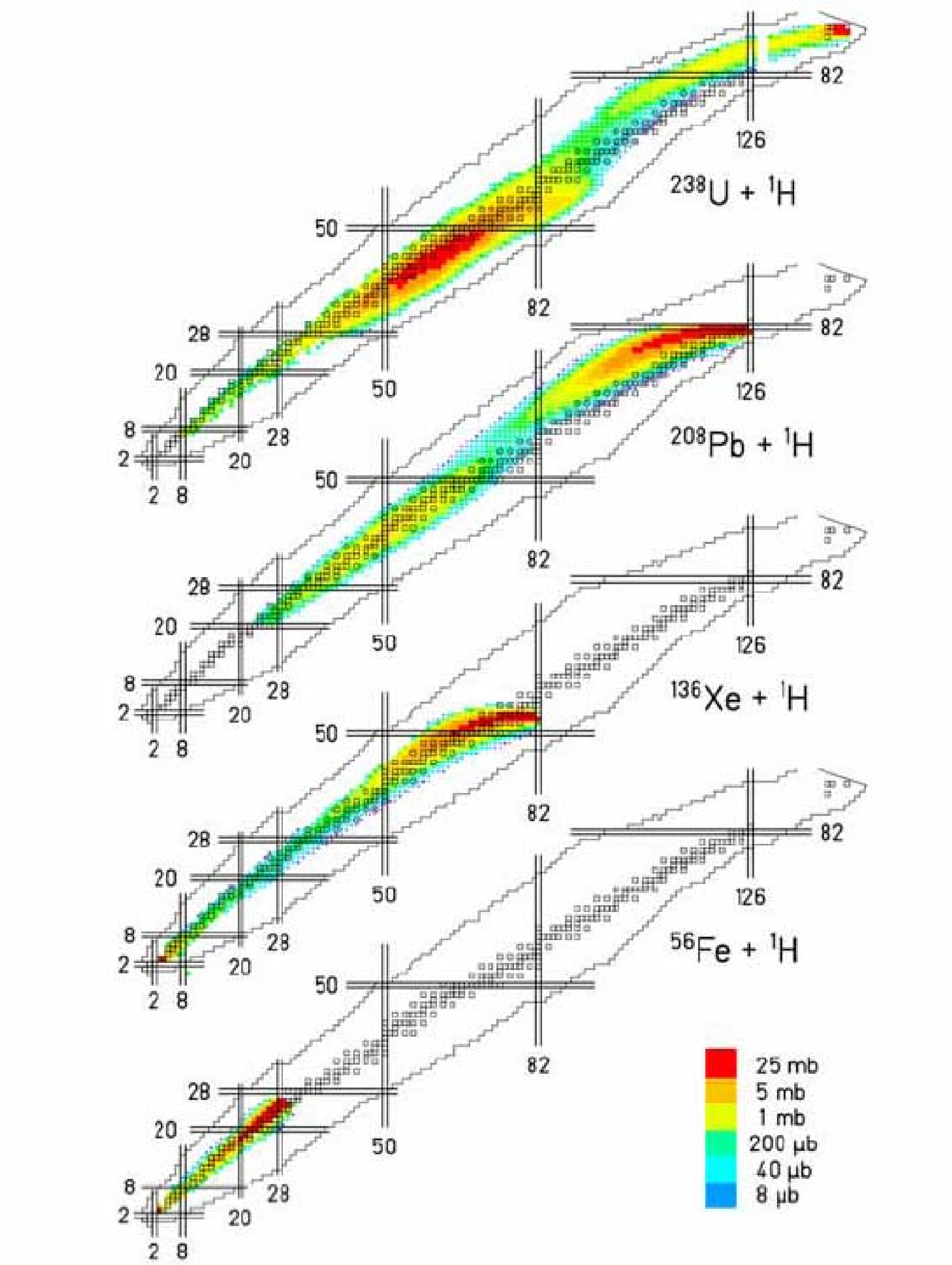

Figure 1: Overview on the nuclide production cross sections measured at the fragment separator FRS at GSI for the four systems indicated at the energy of 1·A GeV on a chart of the nuclides. For references, see the text. The colours indicate the production cross sections on the logarithmic scale as defined in the colour scale. In case of ^{208}*Pb+*^{1}*H reaction, the lightest residues (Z< 20) have not been measured.*

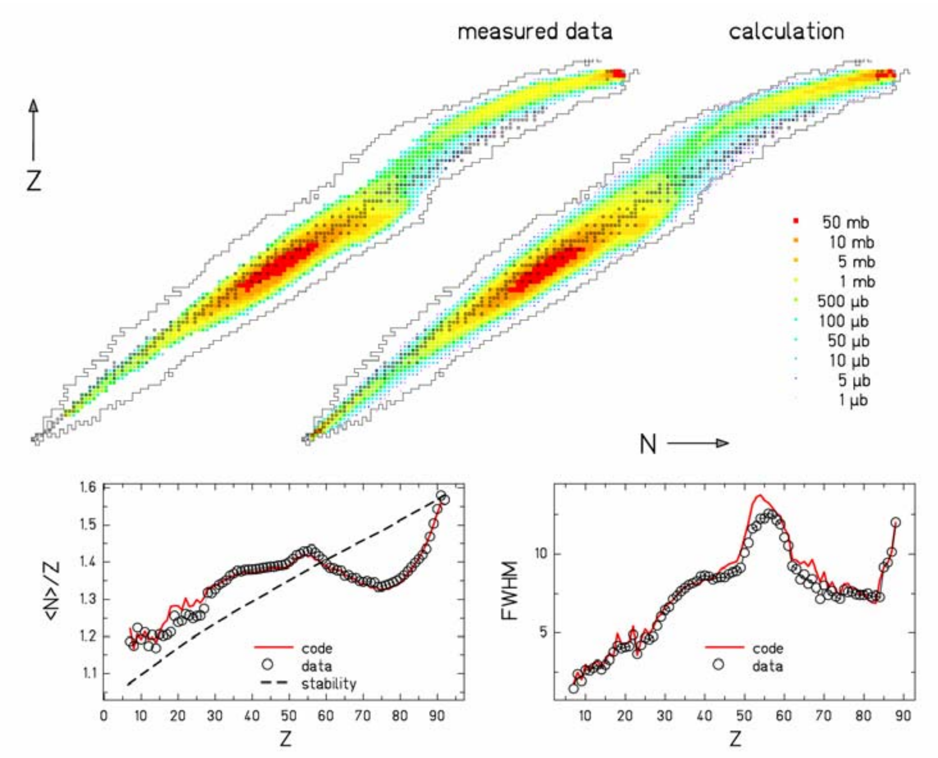

Figure 2: Up – Cross sections for the nuclei produced in 1 GeV proton on ^{238}U: Measured cross sections [12,13,14,15] (left) and prediction of ABRABLA07 [17,18] (right) presented on the chart of the nuclides. Down – Left: Mean neutron-to-proton ratio of isotopic distributions as a function of the atomic number, compared with the stability line (dashed line) and to the ABRABLA07 prediction (solid line). Right: FWHM of the isotopic distributions compared to the prediction of the ABRABLA07 code (solid line).

2.1.2 Heavy-ion collisions

As already mentioned above, a 1 GeV proton beam is considered as the standard option for the driver accelerator. Using different target material, this option allows for producing a large number of isotopes of many elements. However, this standard option might not be optimum in every case. Extended capabilities of the driver accelerator in order to provide additional beam species and more complex technical approaches can result in a benefit for producing nuclides in certain regions of the chart of the nuclides. For these additional solutions knowledge on heavy-ion collisions is necessary.

Heavy-ion collisions show different characteristics for different beam energies: Far above the Fermi energy, fragments are formed as projectile or target spectators in a clean abrasion process. Exploiting specific proton-loss channels in “cold fragmentation” reactions [16] one can reach very neutron-rich isotopes. In the Fermi-energy regime, there is an important exchange of nucleons between the projectile and target nucleus during the reaction, which can be described by adequate nuclear-reaction models. By special tailoring of projectile, target and energy, the production of specific products, e.g. particularly neutron-rich nuclides, may be enhanced.

2.1.2.1 Heavy-ion collisions at relativistic energies

Fragmentation reactions at relativistic energies are usually described as a two-stage process: The first, collision-stage is very fast. It is characterized by the nucleon-nucleon collisions, which are estimated to occur on the time scale of the order of 10 fm/c. After the primary collisions, the distorted nuclear system evolves towards the thermalisation of the nucleonic motion (≈100 fm/c). When the thermalisation is completed, the remnant nucleus can be considered as a compound nucleus. The situation after the first-stage processes is fully described by the parameters of the compound nucleus, i.e. its composition in *A* and *Z*, thermal excitation energy, angular momentum, and linear momentum. They define the starting point of the de-excitation process. Once the thermalisation of the nucleonic motion is reached, the second stage starts, where the statistical de-excitation is treated. At first the system expands (≈100 fm/c). Depending on the temperature it can experience thermal instabilities and break-up into several pre-fragments or evolve as a single compound nucleus. Later on, the system starts its long (up to $\approx 10^7$ fm/c) sequential de-excitation process – consisting of emission of small-nuclei, particles and gammas – which eventually leads to the cold remnant fragment, which is experimentally observed. In case of heavy nuclei, in each de-excitation step fission is also a possible competitive decay channel. The final, observed fragments carry the signatures of both stages of the reaction process.

During the EURISOL Design Study phase, fragmentation reactions at relativistic energies have been systematically investigated in reactions induced by ^{129,136}Xe beams at 1000·*A* MeV, 500·*A* MeV and 200·*A* MeV, impinging different target materials, see Ref. [19]. The isotopic composition and production cross section of the residual nuclei obtained with the Fragment Separator at GSI (details on the experimental technique and data-sorting procedure can be found in e.g. Refs. [11, 12, 14]) made it possible to investigate the role of the projectile energy and isospin as well as the nature of the target in the production of final residual nuclei. Moreover, beams of ^{238}U, ^{208}Pb and ^{136}Xe impinging into beryllium targets at 1000·*A* MeV were also used to specifically investigate the production of neutron-rich nuclei approaching the r-process waiting points at *N*=126 and *N*=82 [19].

The isotopic distributions of the production cross section of projectile residues close in mass number to the projectile nucleus have been investigated in the reactions of ^{136}Xe+Pb, Ti, Be, H all at 1000·*A* MeV, see Figure 3.

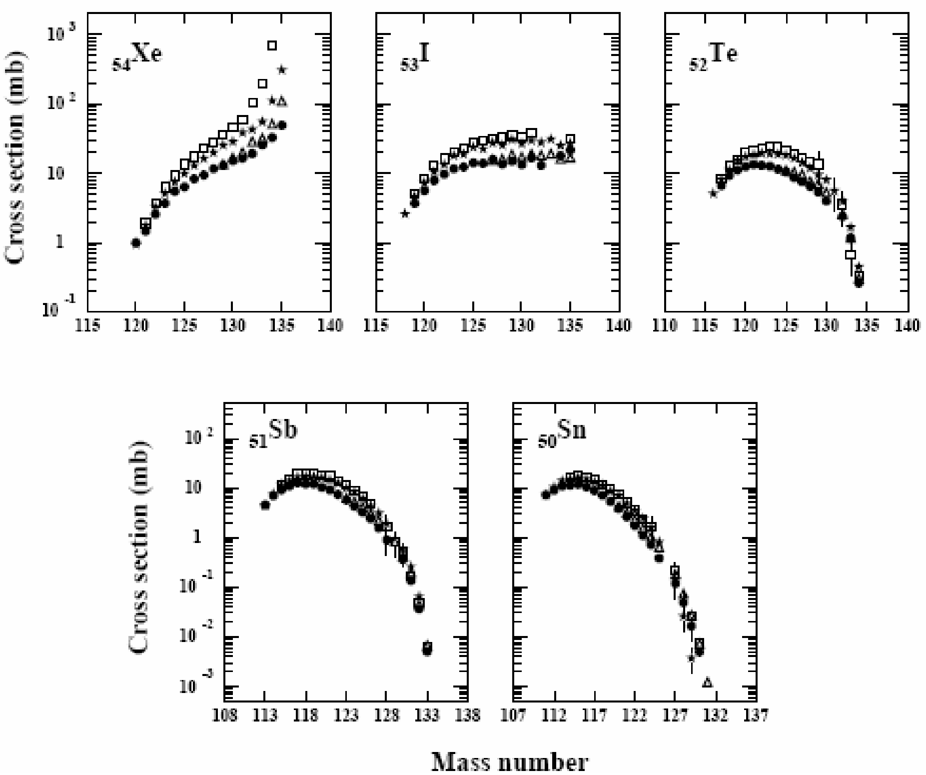

Figure 3: Isotopic distributions of several projectile fragments formed in reactions of ^{136}Xe beam at 1000·A MeV with lead (open squares), titanium (stars), beryllium (open triangles) and hydrogen (circles) target.

The figure shows a clear increase in the production of final resides with target mass number. This effect is especially evident for residual nuclei differing only a few nucleons relative to the incoming beam, and is caused by different total interaction cross sections as predicted by Glauber model [20]. Moreover, in case of lead target, for residual nuclei produced in few neutron removal channels strong influence of Coulomb excitation process enhances additionally the final production cross sections.

Influence of the projectile neutron-to-proton (*N/Z*) ratio on the characteristics of final residues has been studied in the fragmentation reactions of ^{124}Xe, ^{129}Xe and ^{136}Xe, see Figure 4. Difference in the width of isotopic distributions of projectile residues is clearly seen: Reactions with projectiles having larger values of *N/Z* lead to larger widths and higher mean values of isotopic distributions of final residues close in mass to the projectile. The similar conclusion has been obtained in Ref. [21].

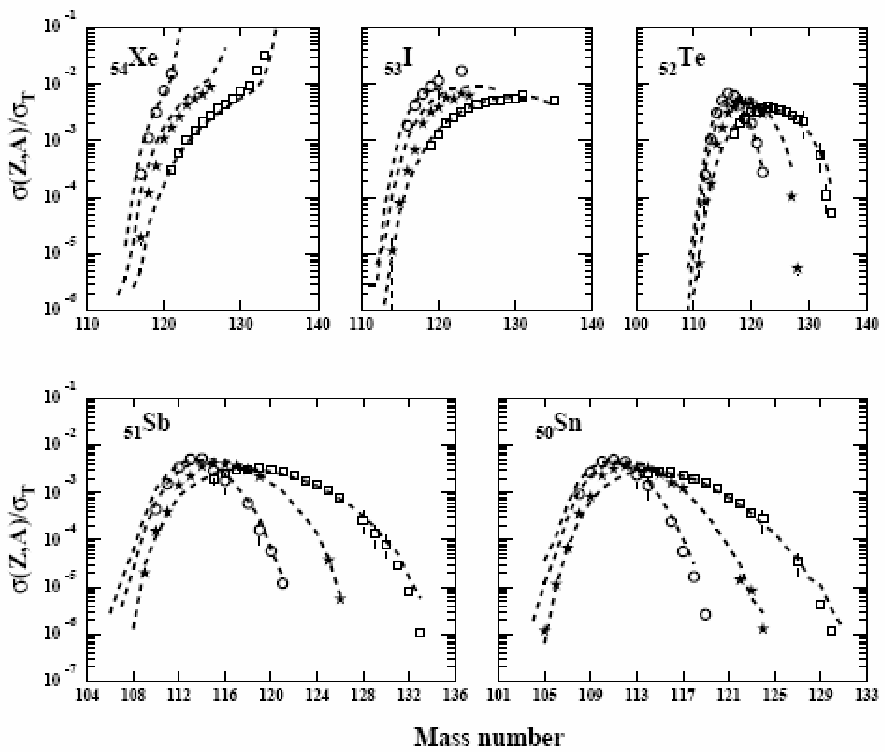

Figure 4: Isotopic distributions of several residual nuclei produced in projectile fragmentation of ^{124}Xe (1000·A MeV) + Be (circles), ^{129}Xe (750·A MeV) + Al (stars) and ^{136}Xe (1000·A MeV) + Be (squares). Dashed lines correspond to the predictions of reaction model ABRABLA.

In Figure 4, the measured data are also compared with the predictions of the ABRABLA reaction model; agreement between measured and calculated data is more than satisfactory.

The projectile energy was the next parameter whose influence has been studied [19]. To this goal, data measured in the fragmentation reaction ^{136}Xe+Ti at 200·*A* MeV, 500·*A* MeV and 1000·*A* MeV have been investigated, see Figure 5. From this figure, it is evident that some of the isotopic distributions of residual nuclei produced in peripheral collisions show a clear dependence on the projectile energy. In particular, for residual nuclei close in mass number to the projectile, e.g. caesium, xenon and indium isotopes, the final cross sections increase inversely with the energy of the projectile. Lighter residual nuclei, like tin isotopes do not show any energy dependence. The reason for this energy dependence of the production cross section of the highest-*Z* products is the charge-exchange mechanism whose strength increases with decreasing the projectile energy [22]. Thus, we can conclude, that for neutron-deficient residual nuclei close in mass number to the projectile there is a not negligible enhancement of the final cross sections at the lowest energies. The production of neutron-rich nuclei seems not to be influenced by the projectile energy. Therefore, one can confirm that the production of neutron-rich nuclei is similar down to energies around 200·*A* MeV, while one can expect a higher production of neutron-deficient nuclei close in mass to the projectile at these lower energies.

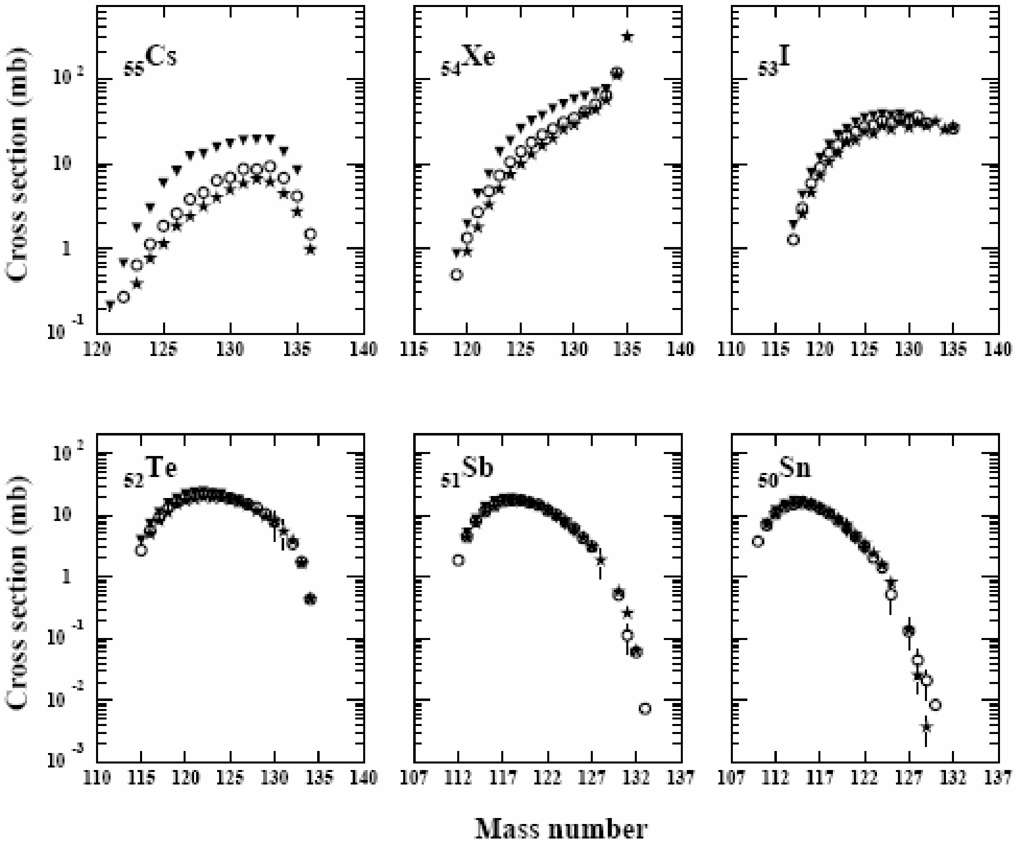

Figure 5: Experimental cross sections of residues produced in projectile fragmentation reactions ^{136}Xe+Ti at 1000·A MeV (stars), 500·A MeV (open dots) and 200·A MeV (triangles).

In Figure 6 the measured cross sections of the proton-removal channels in reactions induced by ^{136}Xe and ^{132}Sn projectiles in a beryllium target around 1000·*A* MeV are shown. The proton-removal channels correspond to the most neutron-rich nuclei that can be produced in fragmentation reactions. These are reaction channels where the projectile nucleus mostly loses protons in the interaction with the target and, at the same time, deposits only little excitation energy, allowing for the evaporation of a few neutrons [16]. This reaction channel leads then to the production of the most neutron-rich nuclei that can be produced in the fragmentation of a given projectile nucleus. Obviously, the production of the most neutron-rich final residues relies on large fluctuations in the proton-to-neutron ratio of the abraded nucleons and in the excitation energy gained by the projectile pre-fragment in the abrasion process. In this scenario, the most extreme case corresponds to the proton-removal channels where only protons are abraded and the excitation energy gained remains below the neutron-evaporation threshold. In the two reactions investigated here the proton-removal channels are located along the *N*=82 line. In both cases the measured cross sections are compared to the predictions obtained with the code COFRA[2] [16] and with the EPAX parameterization [23]. The EPAX formula in general provides a good description of the production cross sections of neutron-deficient fragmentation residues [24]. In the present case, EPAX describes rather well the production cross sections of residual nuclei not too different in mass number from the projectile. However, for residual nuclei with a large neutron excess EPAX clearly overestimates

---

[2] The COFRA code is available at: www.usc.es/genp/cofra.

the production cross sections. The code COFRA provides a better overall description of the present data. Nevertheless, one can also identify a clear tendency to slightly under-predict the production cross sections of neutron-rich residual nuclei with a large difference in mass number with respect to the projectile, as can be seen in Figure 6. It should be stressed that the predictions of the analytical code COFRA are extremely sensitive to the precise values of the neutron separation energies of the nuclei of interest, and that only decay channel considered in the code is neutron evaporation.

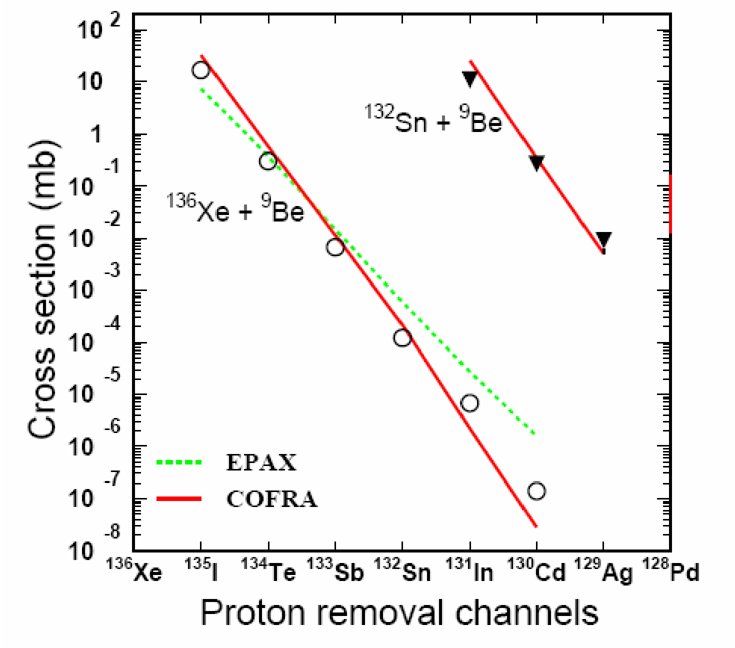

Figure 6: Production cross sections of the proton-removal channels in the reactions ^{136}Xe+Be and ^{132}Sn+Be around 1000·A MeV. The data points are compared to the predictions obtained with two approaches, the COFRA model [16] (solid line) and the EPAX formula [23] (dashed line).

More detailed discussion on the properties of fragmentation reactions at relativistic energies can be found in [19].

2.1.2.2 Heavy-ion collisions at the Fermi energy

In the frame of the EURISOL Design Study, the production rates of neutron-rich nuclei at the Fermi energy were measured with the MARS recoil spectrometer [25] at angles 4 deg and 7 deg in the reactions ^{86}Kr (15·*A* MeV, 10 pnA) + ^{64,58}Ni (2.2 mg/cm^{2}), ^{86}Kr (15·*A* MeV, 10 pnA) + ^{124,112}Sn (2.0 mg/cm^{2}) and ^{40}Ar (15·*A* MeV, 10 pnA) + ^{64,58}Ni (2.2 mg/cm^{2}), ^{40}Ar (15·*A* MeV, 10 pnA) + ^{124,112}Sn (2.0 mg/cm^{2}). These data, together with the other available experimental data from nucleus-nucleus collisions at beam energies from the Coulomb barrier up to 70·*A* MeV and various projectile-target asymmetries have been investigated in details [26]. It was shown, that the scenario involving pre-equilibrium emission in the early stage of the reaction followed by deep-inelastic transfer or incomplete fusion leads to consistent agreement in most of the cases. The participant-spectator scenario starts to play role at energies around 50·*A* MeV for very asymmetric projectile-target combinations. At beam energies around and above 50·*A* MeV there are signals of the mechanism of neutron loss (via dynamical emission) preceding the thermal equilibration of the massive projectile-like fragment. At beam energies below 10·*A* MeV, deep-inelastic transfer appears to be the dominant reaction mechanism, with contribution from the possible extended evolution of nuclear profile in the window (neck) region, mostly in the case of heavy target nuclei.

While at relativistic energies the target composition does not play the major role (see previous section), at the Fermi energy with a proper choice of the target nucleus one can considerably enhance production of wanted exotic product. As an example, in Figure 7 are shown production cross sections of several nickel isotopes measured in the reactions of ^{86}Kr beam with ^{112}Sn and ^{124}Sn target, both at 25·*A* MeV [27]. Influence of the target nucleus is clearly seen.

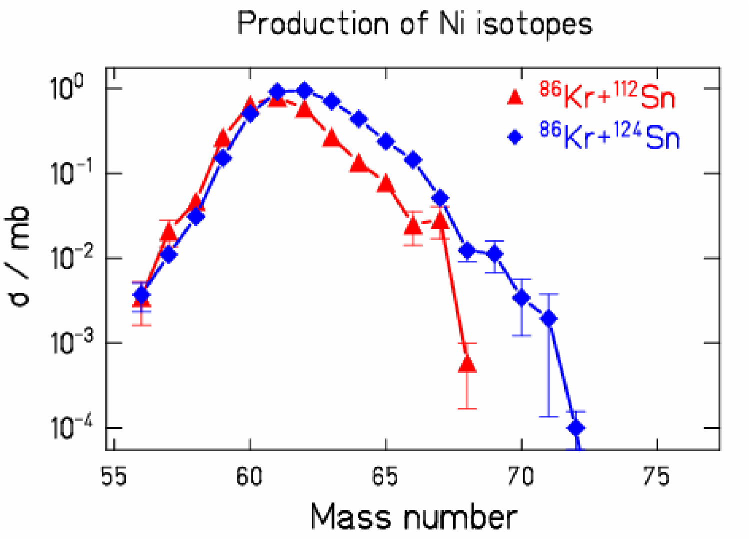

Figure 7: Production cross sections of nickel isotopes in the reactions ^{86}Kr+^{112}Sn (triangles) and ^{86}Kr+^{124}Sn measured at 25·A MeV at 4 degrees [27].

The measured data have been used to test and benchmark the PE+DIT/ICF+SMM model simulations which are based on the pre-equilibrium emission followed by either deep-inelastic transfer or incomplete fusion followed by de-excitation using statistical model of multifragmentation [26]. The model calculations were able to predict measured cross section very reasonably (for more details see [26]). After that, using the model simulation the best-suited energy in the Fermi regime for producing neutron-rich nuclei has been studied. Calculations, see Figure 8, showed that from the point of view of production cross sections the projectile energies around 15·*A* MeV may be close to the optimal energy for producing neutron-rich nuclei at Fermi energy.

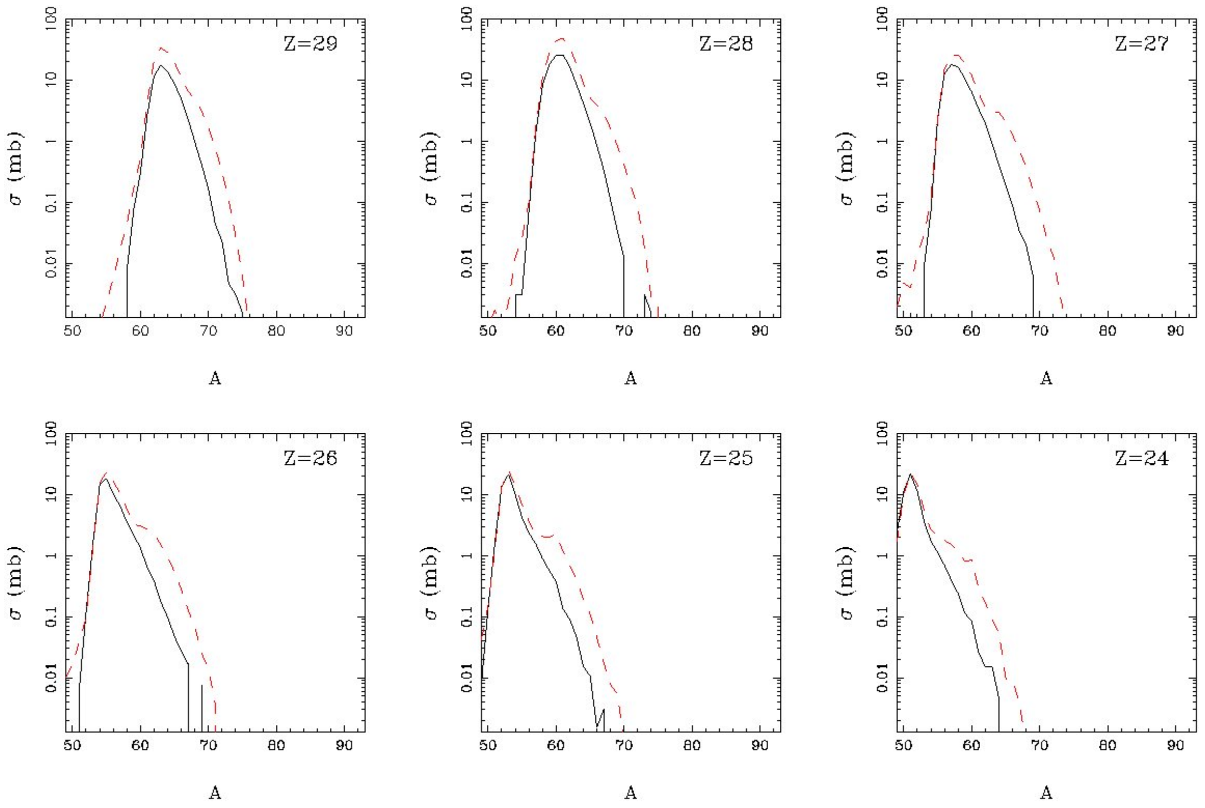

Figure 8: Calculated PE+DIT/ICF+SMM [26] total mass yield curves (corrected for the angular, azimuthal and momentum acceptance of the MARS spectrometer) from the reaction ^{86}Kr+^{64}Ni at 15·A MeV (dashed line) and 25·A MeV (solid line).

More detailed discussion on fragmentation reaction at the Fermi energy can be found in [26].

2.1.3 Fission

Neutron-rich nuclei in the mid-mass region are best produced by fission of a heavy neutron-rich nucleus like ^{238}U. In case of the high-power target option, due to the deposition of the primary-beam energy in the converter target and the concentration of the production on a very limited number of nuclides, one can obtain very high in-target production rates. Best conditions for very high secondary-beam intensities by the ISOL method are provided for nuclides around ^{132}Sn. The double shell closure is responsible for several peculiarities:

1. High production yields in the heavy fission-fragment group go in line with an enhancement of the N/Z ratio due to strong charge polarization.
2. Long half-lives extend to rather large values of the neutron excess.

Fortunately, the mostly produced elements of the heavy fission-fragment group (tin to lanthanum) can be extracted from the production target with rather good efficiencies by the ISOL method. In addition, their long half-lives allow for using rather large target volumes, which are connected with long extraction times, without introducing excessive decay losses. On the contrary, the nuclides in the light fission-fragment group are less favoured: Firstly, they are less neutron-rich; secondly, they have shorter half-lives. However, also here the elements from zinc (Z = 30) to strontium (Z = 38) can be extracted from the production target with rather high efficiencies by the ISOL method. However, moderate target volumes should be used in order to limit the decay losses.

In order to get realistic results on the nuclide production in fission, one needs reliable models with high-predictive power. Fission is very complex process, whose characteristics depend on the entrance channel, e.g. kind and energy of projectile, as well as the on nuclear-structure properties (e.g. shell effects, collective enhancement, pairing correlations) and viscosity of nuclear matter. Many different approaches for describing the fission process have been developed along the years. Theoretical models are, generally, not precise enough and in most of the cases, due to long computing times, not practicable in applications. Empirical models, on the other hand, have only a limited predictive power, especially far from regions covered by experiments. Therefore, the benchmarking of fission models against available data and their improvement was one the first steps that have been underdone in the frame of the EURISOL Design Study. Moreover, using a novel method developed at Jyväskylä independent fission product yields in particle-induced fission below Fermi energy have been measured [28] and used as well for model benchmarking.

This novel method [28] is based on identifying and detecting fission products by direct counting after separation in the purification trap of the JYFLTRAP [29]. It takes advantage of the fact that a Penning trap can be used as a precision mass filter, which allows an unambiguous identification of the fission fragments with a typical mass resolving power of 10^5. Due to the ion production mechanism of IGISOL only directly produced ions are detected and hence independent yields are measured. The method was tested with 25 MeV and 50 MeV p-induced fission of ^{238}U. The data are internally reproducible and the results for Rb and Cs yields in 50 MeV proton induced fission agree with previous measurements. In addition to proton-induced fission, yields for 25 MeV deuteron-induced fission of ^{238}U were measured for selected elements [30]. More details can be found in Ref. [31].

Available data on particle-induced fission at energies below the Fermi energy have been used to benchmark and develop the Jyväskylä fission model FIPRODY [32]. FIPRODY is a generalized model for the description of the prompt fission neutron spectra and multiplicities at neutron and proton energies up to about 100 MeV. The three main emission mechanisms considered are the pre-compound emission, the pre-scission particle evaporation before the saddle point and at descent to the scission point, and the emission from excited fission fragments. The two-component exciton model is used for the description of the pre-equilibrium stage of the reaction. The time-dependent statistical model with inclusion of the nuclear friction effects describes particle evaporation starting just after the pre-compound emission stage and lasting for the duration of the evolution of the compound nucleus toward scission. The fragment mass distribution and fission fragment kinetic and excitation energies are determined from the properties of the composite system at the scission point. The particle spectra from the fission fragments are calculated within the statistical approach. These spectra are then transformed into the laboratory rest frame using the calculated fragment kinetic energies and are averaged over the calculated fragment mass distributions. Details of the model are given in Ref. [32]. In Figure 9-Figure ***10*** some examples of FIPRODY calculations are given.

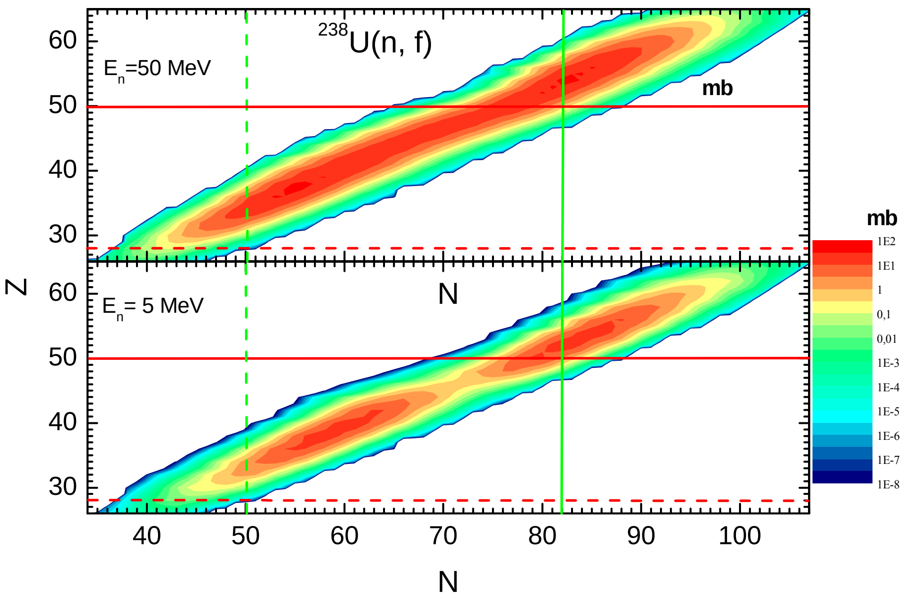

Figure 9: Calculated fission product formation cross sections in the neutron-induced fission of ^{238}U at E_n=5 MeV (lower part of figure) and 50 MeV (upper part of figure).

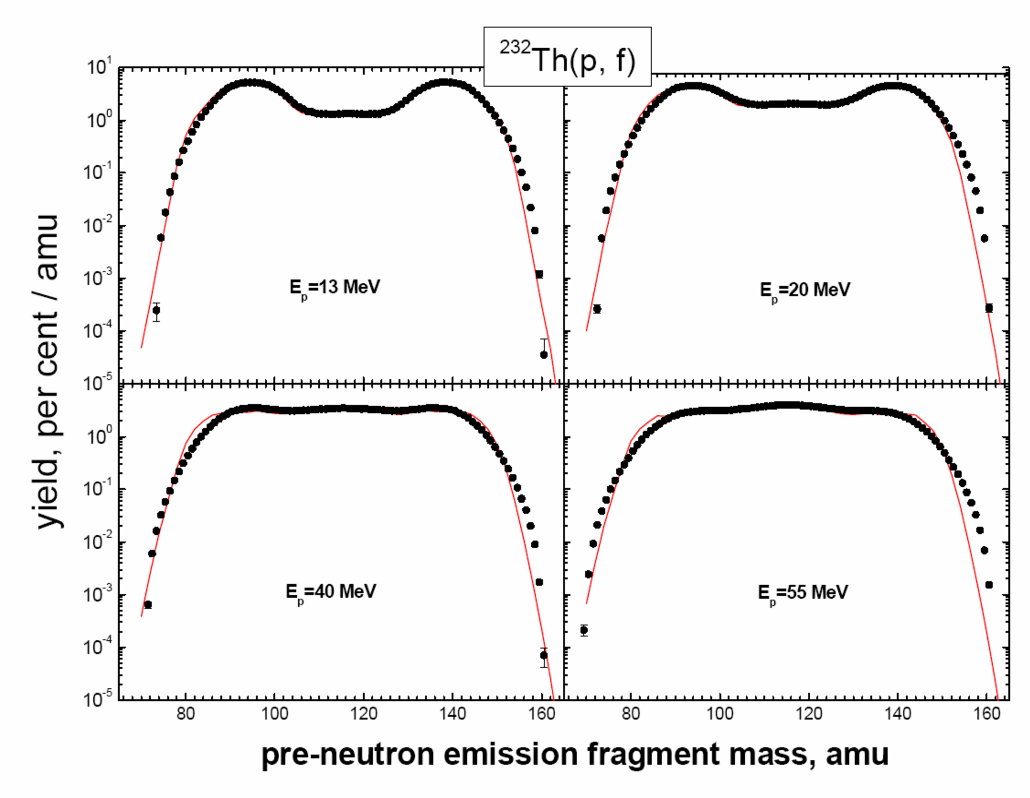

Figure 10: Calculated (lines) and measured (symbols) mass distributions in the proton-induced fission of ^{232}Th at different proton-beam energies.

The GSI evaporation-fission ABLA-PROFI code system has been extended to include the production of intermediate-mass fragments (IMFs) with $Z \geq 3$ from binary reactions (extremely asymmetric fission) [14]. This reaction mechanism has been used very successfully for the production of very neutron-rich isotopes of elements below $Z = 20$ in uranium targets at ISOLDE. The particle emission during the descent from saddle to scission has been modelled on the basis of three-dimensional Langevin calculations. The role of transient effects on the fission probabilities and on the mass distributions of fission fragments was analyzed from experimental data obtained in spallation-fission experiments [33,34]. As the output of the code one obtains the following information: Nuclide production cross-sections and velocities of IMFs, fission residues, evaporation residues; Pre-saddle, saddle-to-scission and post-scission multiplicities and kinetic-energy spectra of neutrons and light charged particles ($Z \leq 2$); Isotopic, isobaric and isotonic distributions of fission residues (both before and after particle emission).

Apart from these improvements, the following ingredients are now also considered in the ABLA07 code [18]: Simultaneous emission of intermediate-mass fragments in the break-up process, thermal expansion of the source, change of the angular momentum due to particle emission, influence of initial conditions (e.g. deformation) on the time-dependent fission width, double-humped structure in fission barriers of actinide nuclei and influence of symmetry classes in low-energy fission. All these features have direct or indirect influence on the nuclide production by fission in spallation reactions.

PROFI - the semi-empirical fission model for the prediction of the nuclide distribution in fission is imbedded in the de-excitation code ABLA07; preliminary version of the PROFI model has been published in [35,36], updated version is topic of a forthcoming publication (see also [37]). When the system passes the fission barrier and proceeds to fission, it is characterised by mass and atomic number, excitation energy and angular momentum. In the model, probabilities to evaporate neutrons and light charged particles on the descent from saddle to scission are calculated, and the probability that the system ends up in one of the many possible configurations characterized by two fission fragments with atomic numbers $Z_{1,2}$, mass numbers $A_{1,2}$, kinetic energies $E_{1,2}^{kin}$, excitation energy $E_{1,2}^{exc}$ is predicted. After the two fission fragments are formed, their deexcitation is followed until their excitation energies fall below the lowest particle-emission threshold. The most salient features of the PROFI model are formulated as a rather peculiar application of the macroscopic-microscopic approach to nuclear properties. In the consideration of the properties of the fissioning system at the saddle configuration, one attributes the macroscopic properties of the nuclear potential-energy surface to the strongly deformed fissioning system, while the microscopic properties are attributed to the qualitative features of the shell structure in the nascent fragments [38]. This way, the macroscopic and the microscopic properties are strongly separated, and the number of free parameters is independent from the number of systems considered. This makes extrapolations in experimentally unexplored regions more reliable. With one and the same set of the model parameters one is able to reproduce a large variety of experimental data on mass, nuclear-charge, TKE and neutron-multiplicity distributions in low- (e.g. Figure 11-Figure ***12***) and high-energy fission (e.g. Figure 2).

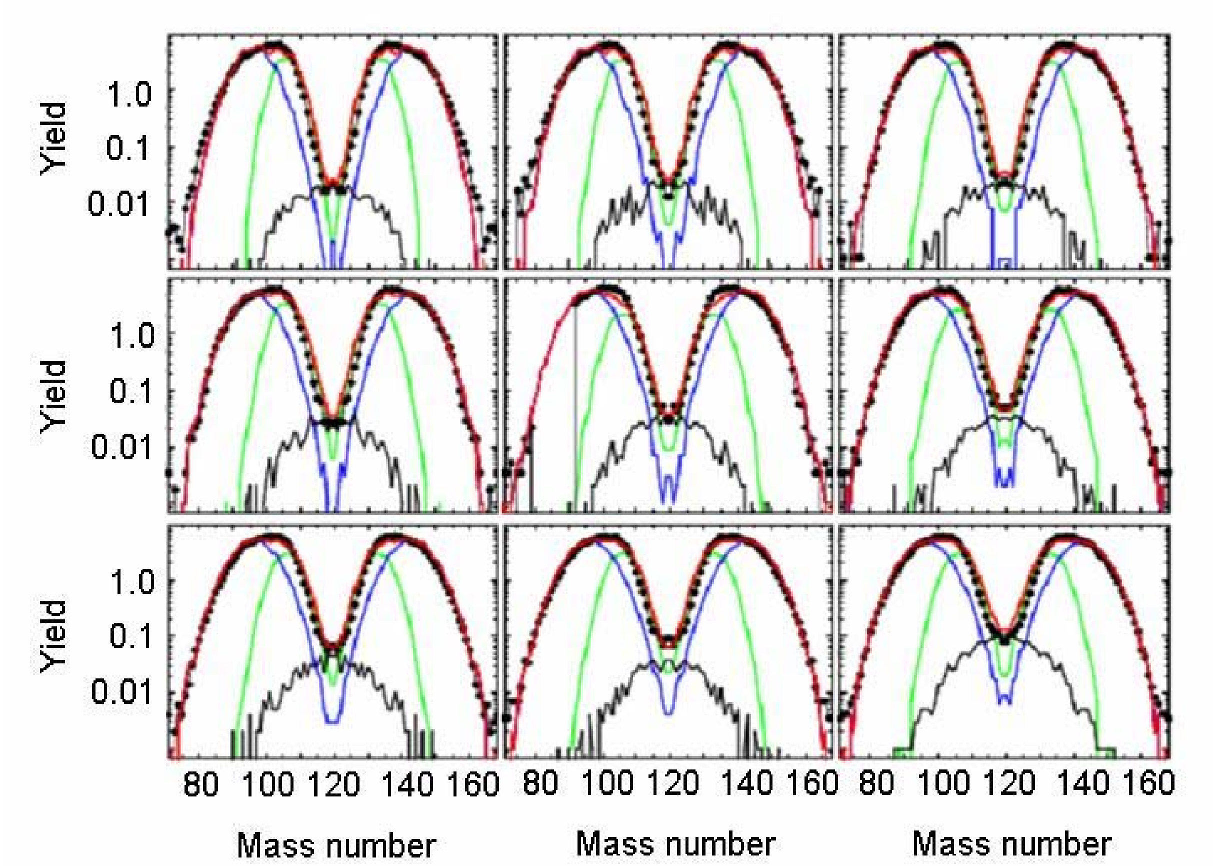

Figure 11: Calculated mass distributions (red line) for neutron-induced fission of ^{238}U in comparison with experimental data (black symbols) [39, 40] for different values of the excitation energy above the fission saddle (0.2, 1.0, 1.5, 2.0, 2.5, 3.0, 3.5, 4.0 and 6.0 MeV going from the upper left corner) of the composite system ^{239}U. The calculated individual contributions of the different fission channels are shown in addition: Standard 1 (green), standard 2 (blue), and superlong (black).

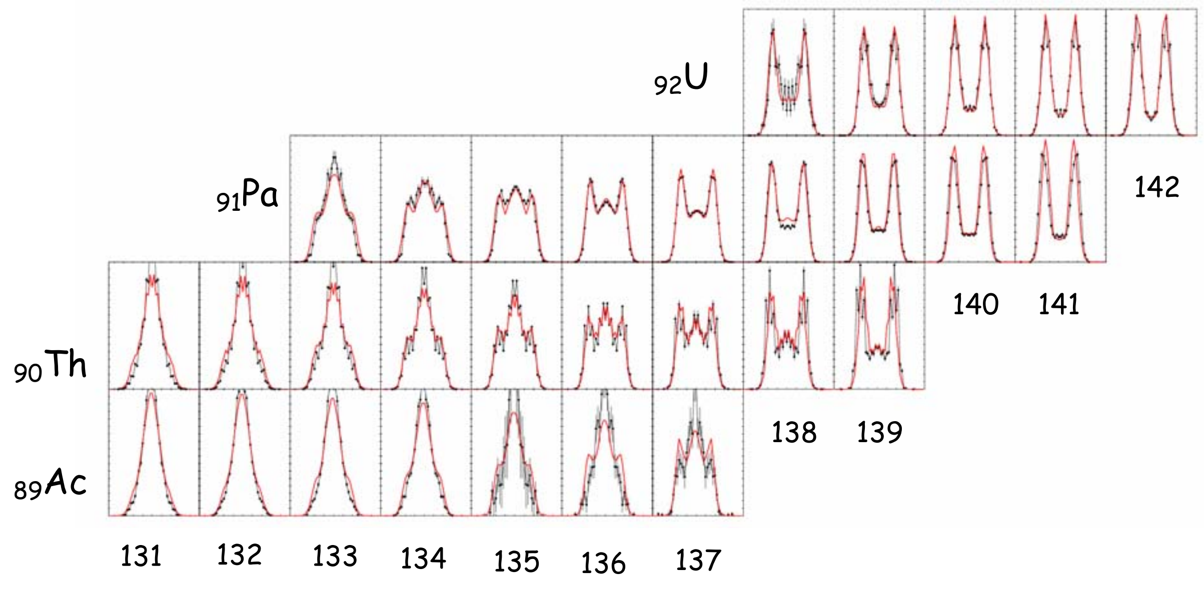

Figure 12: Comparison between measured (black dots) and calculated (red line) fission-fragment nuclear-charge distributions in the range Z = 24 to Z = 65 from ^{220}Ac to ^{234}U in electromagnetic-induced fission shown on a chart of the nuclides. Experimental data are taken from Ref. [41]

2.2 Additional scenarios

As an ISOL-based facility, EURISOL has to face a few technical conditions like a limited choice of the target material, element-dependent overall efficiencies, and decay losses for short-lived species.

The two baseline proton-driver options, direct target and high-power fission target, rely on the use of a thick target, where the radioactive species are produced by the primary protons and by the secondary neutrons, respectively. Thus, it is the same material in which the radioactive species are produced and from which they have to be extracted. For this reason, at present only a limited number of elements is well suited as a component of an ISOL target, e.g., due to the required thermal stability. In Figure 13 a graphical presentation of different target materials used at ISOLDE and some other ISOL-type facilities that has been compiled and discussed by Ulli Köster in 2001 [42] is presented. This figure illustrates that important gaps exist between the different elements used as ISOL targets. As a general rule, one may conclude that these gaps usually extend over about 10 elements. The restrictions can be even more severe, because there are further restrictions on the target material for specific elements to be extracted as secondary beams, e.g., due to conditions on chemical reactivity or vapour pressure of the target material. These limitations are explicitly discussed in Ref. [42]. This implies some boundaries on the optimization of the target material in view of nuclear-reaction aspects governing the production of specific secondary beams. It has to be stressed that these limitations can be overcome in some cases by dedicated research and development that have also been made during the EURISOL_DS Project. However, the general impression given by Figure 13 will, to a certain extent, remain valid also for the operation of EURISOL.

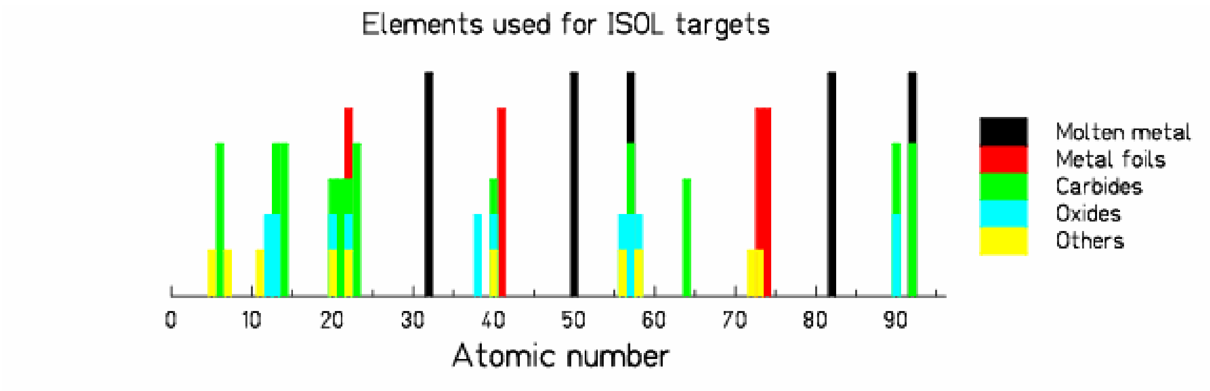

Figure 13: Graphical presentation of the elements used for ISOL targets (data from ref. [42]). The columns are drawn with different heights for graphical reasons only.

Additional limitation comes from the fact that not all elements can be extracted from ISOL targets with high overall efficiencies. Even for sufficiently long-lived isotopes, which are not affected by decay losses during the diffusion and effusion processes occurring in the target–ion-source system, losses may occur in the different stages of the extraction process. Some elements, e.g., the refractory elements, have even so low volatility that they are extracted with very low efficiencies or not observed at all. In Figure 14 are shown presently available beams at SC-ISOLDE [43]. It gives a good impression on the possibilities and limitations of the ISOL method. It is particularly penalizing that the elements between ytterbium (*Z*=39) and palladium (*Z*=46) and elements around phosphorus (*Z*=15) and chromium (*Z*=24), for which very neutron-rich isotopes can be produced by fission of actinides, have very low overall efficiencies.

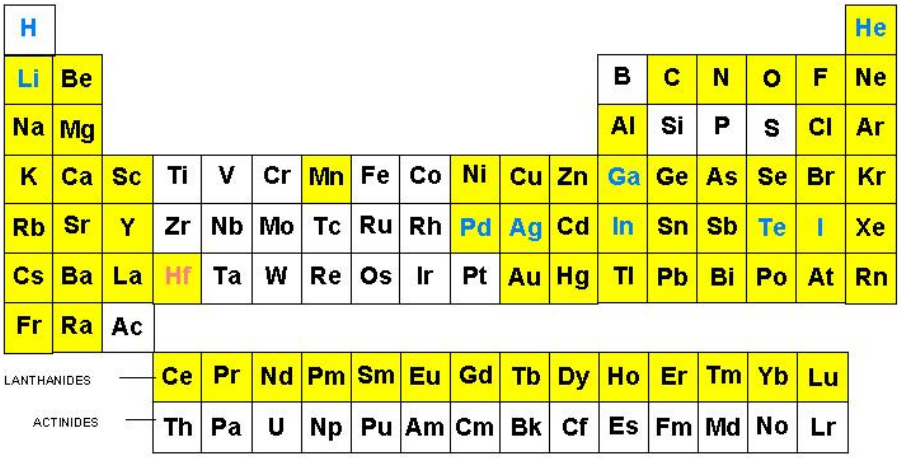

H																	He
Li	Be											B	C	N	O	F	Ne
Na	Mg											Al	Si	P	S	Cl	Ar
K	Ca	Sc	Ti	V	Cr	Mn	Fe	Co	Ni	Cu	Zn	Ga	Ge	As	Se	Br	Kr
Rb	Sr	Y	Zr	Nb	Mo	Tc	Ru	Rh	Pd	Ag	Cd	In	Sn	Sb	Te	I	Xe
Cs	Ba	La	Hf	Ta	W	Re	Os	Ir	Pt	Au	Hg	Tl	Pb	Bi	Po	At	Rn
Fr	Ra	Ac															
LANTHANIDES			Ce	Pr	Nd	Pm	Sm	Eu	Gd	Tb	Dy	Ho	Er	Tm	Yb	Lu	
ACTINIDES			Th	Pa	U	Np	Pu	Am	Cm	Bk	Cf	Es	Fm	Md	No	Lr	

Figure 14: Elements (marked in yellow) available at SC-ISOLDE as beams [43]. If the element is marked in blue only neutron rich isotopes are produced, while red stands for only neutron deficient ones.

High primary reaction rates are reached by using rather large target volumes. Unfortunately, this leads almost inevitably to long transport times. Figure 15 illustrates the restrictions on the length of isotopic chains to be prepared as secondary beams, which are imposed by the limitations on half-lives longer than 100, 10, and 1 s, respectively. Although the figure is incomplete, because measurements of shorter half-lives are scarce, the figure gives an impression on the steep decrease of the nuclear life times with increasing distance from the valley of beta stability.

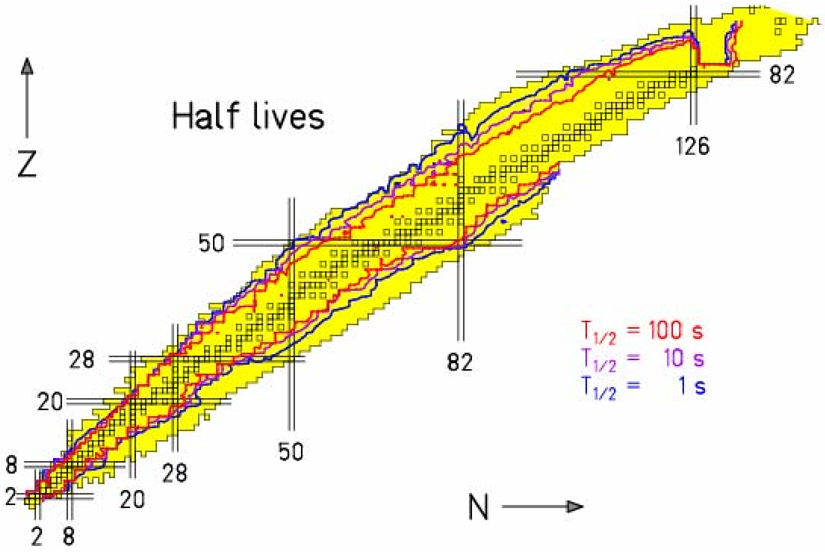

Figure 15: Chart of the nuclides. The yellow area covers the nuclides observed up to now. Black open squares denote stable nuclides. The contour lines mark regions of equal measured nuclear life times: 1, 10 and 100 seconds. On the neutron-rich side, the contour lines are missing above Z = 65, since the experimental data for that region do not reach short half-lives.

In order to enlarge the discovery potential of EURISOL additional options have been considered.

2.2.1 Additional options of driver accelerator

The secondary-beam production in the EURISOL baseline option (1 GeV proton beam 3-4 MW on a converter target and 100 kW on a direct target) allows for producing a large number of isotopes of many elements using different target materials. However, extended capabilities of the driver accelerator in order to provide additional beam species and more complex technical approaches might result in a benefit for producing nuclides in certain regions of the chart of the nuclides. During the EURSIOL Design Study phase, this question has been investigated in a systematic way. For this purpose, the benefit of extended capabilities of the driver accelerator has been considered in connection with a quantitative discussion of nuclear-reaction aspects and the technical limitations of the ISOL method. From this study, the following results have been obtained (for more details, see [44]):

With respect to the baseline option, the following cases could provide substantial benefits:

- A 2 GeV $^3He^{2+}$ beam would fill the gaps in the nuclide production given by the limited choice of ISOL target materials. As an example, Figure 16 compares the maximum obtainable in-target production rates for the isotopic chain of rhenium with 1 GeV proton beam or 2 GeV ^3He beam. The beam power has been normalized to 100 kW for protons and 50 kW for ^3He. It is obvious that there is a clear advantage for the production of rhenium in favour of the 2 GeV ^3He option by up to a factor 4, if the same thermal power density in the production target is considered. The gain decreases slightly towards the neutron-rich wing of the isotopic distribution. Of course, the final judgement on the benefit of a 2 GeV ^3He beam depends on the size of the gaps in the choice of suitable target material for EURISOL. If suitable targets can be provided by future developments all over the range of elements of interest with a maximum distance of 10 units in *Z*, then there will be no gain by the 2 GeV ^3He option with respect to the 1 GeV proton design. On the contrary, if the gaps of about 20 units in *Z* remain, then there is a clear advantage of up to a factor 4 for the 2 GeV ^3He option for certain elements due to the extended mass range produced.

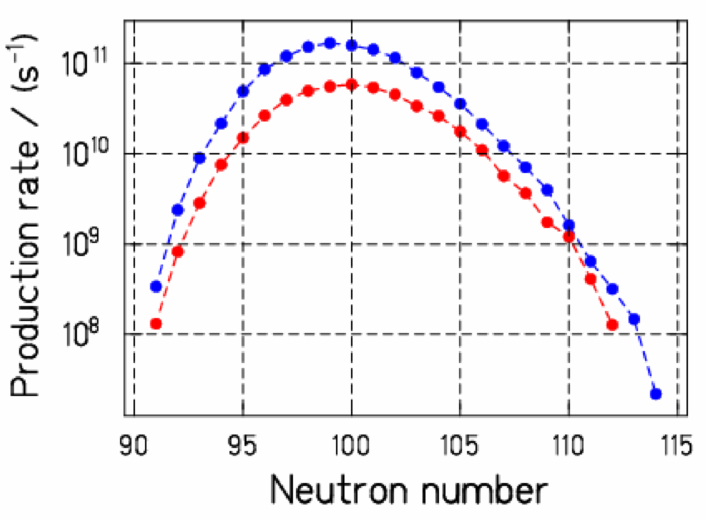

Figure 16: In-target production rates of rhenium isotopes (Z = 75), in the spallation-evaporation reaction induced by 1 GeV protons (red symbols) and 2 GeV ^3He (blue symbols) in a uranium-carbide target. The assumed beam power is 100 kW in the case of protons, and 50 kW in the case of ^3He. A target thickness of 240 g/cm^2 was assumed, beyond which the production drops significantly in both cases.

- A 2 GeV ^{3}He^{2+} beam would increase the production of neutron-rich isotopes of light to medium-heavy elements ($Z < 30$) by about a factor of 2. This is due to the fact that the production of these intermediate-mass fragments (IMFs) in a fissile target is sensitive to the energy of the incoming beam. In Figure 17 the production cross sections of sodium isotopes calculated with INCL4 [45]+ABLA07 [18] assuming 1 GeV proton-, 2 GeV proton-beam and 2 GeV ^{3}He all impinging in ^{238}U target are shown; also the data measured in the reaction ^{1}H(1 GeV)+^{238}U at GSI are presented [14]. According to these calculations, with 2-GeV protons one can expect an increase in the production cross sections of IMFs by a factor of ~ 4 as compared to the 1-GeV-proton option. Moreover, if one would use ^{3}He beam one could expect ~ 8 times stronger production of IMF as compared to the standard 1-GeV option. The reason for the additional increase of the IMF production cross-sections with the use of ^{3}He projectiles is related to the stronger population of the high-energy tail of the calculated prefragment excitation-energy distribution due to the larger size of the projectile. However, there are no analyzed experimental data yet to confirm this effect. One can conclude that an increase in the primary-beam energy and, additionally, the use of a ^{3}He^{2+} beam could lead to an important enhancement of light, $Z <$ 30, neutron-rich nuclides. If normalized to the same deposited thermal energy, this enhancement amounts to a factor of about 2.

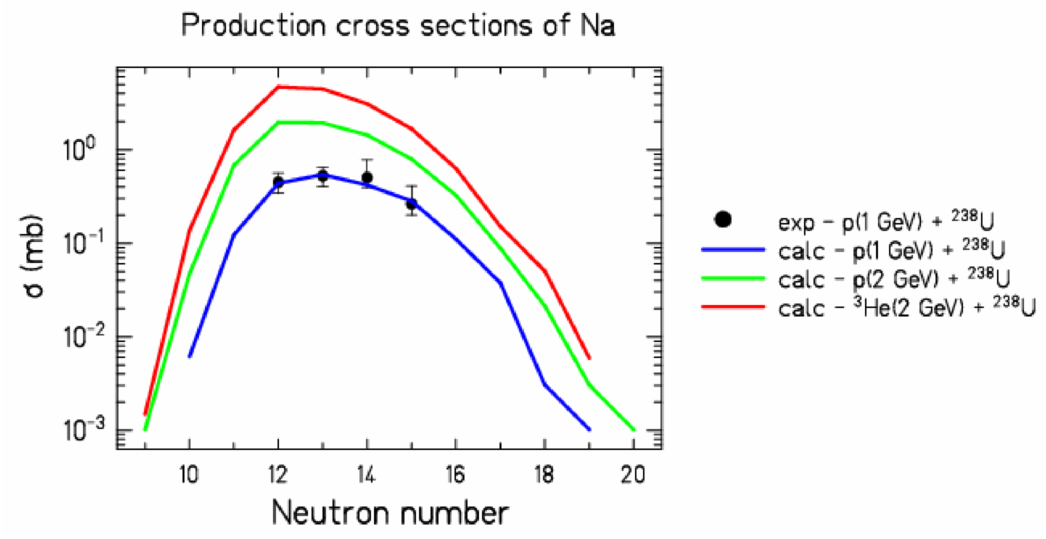

Figure 17: Production cross sections of Na in a ^{238}U target interacting with different beams – 1-GeV protons (blue line), 2-GeV protons (green line) and 2-GeV ^{3}He (red line). Calculations were made with INCL4 [45] coupled to ABLA07 [18]. For comparison, also sodium production cross sections (points) measured at GSI in the reaction ^{1}H(1 GeV)+^{238}U [14] are shown.

- The deuteron-converter option with a primary-beam energy between 40 MeV and 100 MeV provides fission-fragment nuclide distributions with appreciably higher fission yields (normalized to the total number of fission events in the target) for elements between technetium (Z = 43) and indium (Z = 49), below germanium (Z = 32), and above neodymium (Z = 60) compared to the standard EURISOL high-power-target option. However, only part of this advantage can be used, since many of the enhanced elements are poorly or not at all released from ISOL-type targets.
- Fragmentation of heavy-ion projectiles provides higher in-target yields for some neutron-deficient isotopes of light elements and presumably higher overall ISOL efficiencies for short-lived isotopes. It can also be useful to overcome limitations in the choice of the target material in the standard proton-beam option and to divide production target and catcher. The gain factors depend strongly on the

beam energy. This option has been discussed in details by the Target-and-Ion-Source group in the EURIOSL RTD report (Appendix C, Section 2.2.3) [2].

- Due to nucleon-exchange between projectile and target, heavy-ion reactions in the Fermi-energy regime can provide a substantial benefit for the production of neutron-rich isotopes of elements outside the main fission region. However, the quality of such secondary beams would be lower than in other cases. The use of a gas cell may be an alternative, leading to better beam quality, provided that losses will not increase dramatically, which is an open question needing further R&D.

The quantitative conclusions depend on assumptions on the values of some key parameters, e.g. maximum beam intensities or limits on the target heat load. Of course, one should not forget that possible future advance of technological limits, on e.g. currents provided by the ion source or heat load in the target, can strongly influence above-listed conclusions.

2.2.2 Two-step reactions

The high-power target at the future EURISOL facility will take advantage of a extremely high fission rate (~ 10^{16} s^{-1}) for producing medium-mass neutron-rich nuclei with the exception of the refractory elements. In order to overcome this limitation, a two-step reaction scheme has been proposed [7]. Moreover, this method has the advantage of producing even more neutron-rich nuclei as compared to those produced by fission. According to this idea, intense beams of neutron-rich nuclei could be produced reaccelerating non-refractory fission residues, e.g. ^{132}Sn, produced in an ISOL facility. These neutron-rich projectiles could then be fragmented to produce more neutron-rich nuclei covering the refractory gaps.

In order to validate this two-step scheme, a specific experiment was designed and performed at GSI (Darmstadt) [46]. Details on the experiment and data analysis can be found in Ref. [46]. In Figure 18 isotopic distributions of residual nuclei produced in the fragmentation of ^{132}Sn in beryllium target are shown. As it can be seen, very neutron-rich isotopes of In, Cd, Ag, Pd, Rh and Ru with cross sections as low as 10 μb were produced covering the gap of refractory elements in this region of the chart of the nuclides. In the case of In, Cd and Ag the most neutron-rich nuclei that can be produced in the fragmentation of ^{132}Sn corresponding to the one (^{131}In), two (^{130}Cs) and three (^{129}Ag) proton removal channels have been reached. Error bars are dominated by statistical uncertainties.

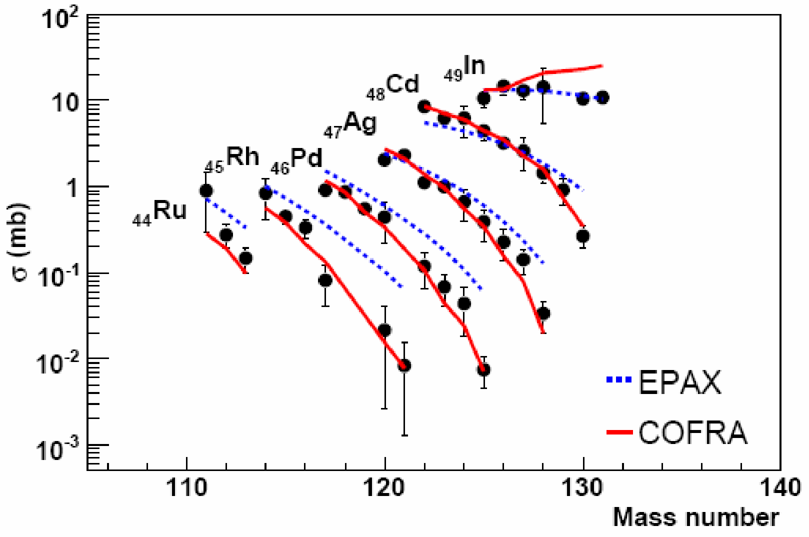

Figure 18: Isotopic distributions of the production cross sections of residual nuclei produced in the fragmentation of ^{132}Sn projectiles in beryllium target.

The good quality of the data obtained in this work made it possible to benchmark different reaction codes describing the production cross sections of fragmentation residual nuclei. In particular, the semi-empirical formula EPAX [23] and a simplified version of the abrasion-ablation model, the COFRA code [16] have been tested, and the results are shown in Figure 18.

These results have been used to estimate the expected production yields in a two-step scenario at EURISOL. In order to do so, one must use not only the measured cross sections in this work but also some assumptions on the productions in the primary target. The numbers used are the following: A total fission rate of 10^{16} s^{-1} in the high-power target, leading to an in-target production of ^{132}Sn of about 10^{14} s^{-1} has been assumed. This production will be reduced by the target release, ionisation and acceleration efficiencies to about 10%, being the expected intensity of re-accelerated ^{132}Sn of 10^{13} s^{-1}. Considering a beam energy of 150·*A* MeV, the optimum thickness for the beryllium fragmentation target would be 500 mg/cm^2, which corresponds to about 50% of the range of the ^{132}Sn in beryllium and a 8 % reaction probability. For a nucleus, which is produced with a cross section of 1 mb, the conversion rate in this target amounts to $3.3{\cdot}10^{8}$ s^{-1}. The expected intensities obtained by fragmentation of the re-accelerated ^{132}Sn are depicted in Figure 19. The cross sections were calculated with the COFRA and the ABRABLA07 codes.

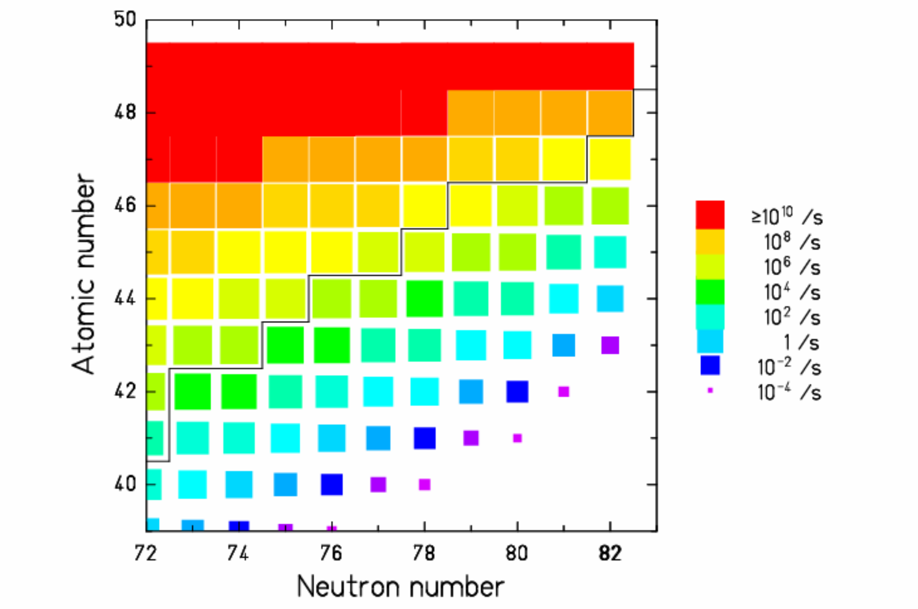

Figure 19: Beam intensities obtained in EURISOL by fragmentation of a ^{132}Sn beam calculated with the COFRA and the ABRABLA07 codes. The ^{132}Sn is assumed to have an energy of 150·A MeV and an intensity of 10^{13}/s. The stair function denotes the limit of known nuclides.

As it can be seen from Figure 19, the fragmentation of intense beams of ^{132}Sn not only covers the region of refractory elements hardly or not at all reachable at ISOL-type facilities but also makes it possible to extend considerably the present limits of the chart of the nuclides. Moreover, this option results in about six orders of magnitude higher production cross sections of nuclei in this region as compared to direct fragmentation of the nearest stabile beam ^{136}Xe, see Figure 6. The present calculations show that this technique will open the possibility for nuclear structure investigations of extremely neutron-rich nuclei with an atomic number down to six units below the one of the projectile. This technique can also be applied with other fission residues having large extraction efficiencies from the ISOL target. The combination of few selected fission residues as fragmentation projectiles will make it possible to produce a large variety of medium-mass neutron-rich nuclei, larger as the one shown in Figure 19.

An important question concerning the two-step option is of course optimum energy of the post-accelerator. Different aspects, e.g. reaction mechanism, charge-state distributions or optimal target thickness, have to be considered in order to decide on the optimal energy of the post-accelerator. Moreover, one has also to consider the costs connected with development and realisation of the post-accelerator. Detailed analysis on the optimal energy of the post-accelerator has been performed in Ref. [46], and here only a summary of the results is given.

The results of this study (see also discussion in Section 2.1.2.1) have clearly shown that the production of neutron-rich nuclei is similar down to energies around 200·*A* MeV, while one can expect a higher production of neutron-deficient nuclei close in mass to the projectile at these lower energies. On the other hand, the Fermi energy domain can be competitive for production of very neutron-rich nuclei around the *N*=50 and *N*=82 shell closures. Of course, to realize this method in practice, specific technical solutions are mandatory, including ion-optical devices with angular acceptance up to 10 degrees, such as superconducting solenoids, and effective event-by-event tagging procedure for an in-flight scenario or a highly effective gas cell for production of high-purity secondary beams.

Another factor influencing optimum energy of the post-accelerator is the charge-state distribution. The evolution of the ionic charge-state distribution as a function of the beam energy is shown in Figure 20 for *Z* = 50. The purity of the secondary beam after a magnetic selection is disturbed by contaminants of different ionic charge states. In particular when fragmentation products on the neutron-rich tail of the production are considered, less neutron-rich products, which are much more abundantly produced, pass the separator too. It depends on the requirements of the specific experiment, how much these contaminants disturb the experimental conditions. In view of the beam purity, an energy of at least 150·*A* MeV would be desirable.

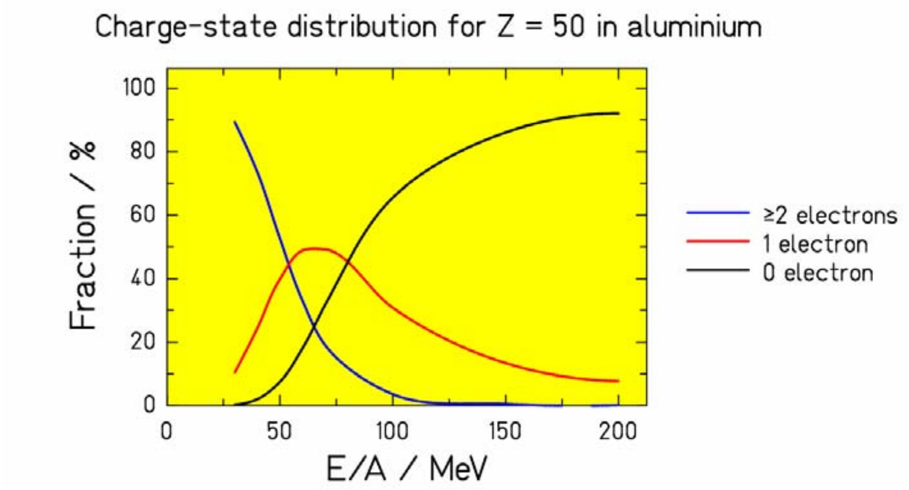

Figure 20: Charge-state probabilities of tin projectiles after a thick aluminium layer as a function of the energy.

The usable target thickness is determined by the range on the projectiles in the target material and therefore by the projectile energy. In this respect the higher the energy the thicker the target that can be used taking into account that a factor of two in energy leads to a factor 3.2 increase in the reaction rate.

All these arguments clearly justify as an optimum value for post-acceleration of 150·*A* MeV. Of course, this should be considered as a maximum value since lower energies would make it possible to use other reaction mechanisms like deep-inelastic reactions for the production of neutron-rich nuclei.

2.3 Transport phenomena

In realistic experimental scenarios thick target are used, and thus this environment has to be modelled with the application of transport codes. Moreover, such calculations can be used to optimize the geometry of target assemblies. This applies in particular to the double-stage target scenario, in which the nuclide production is performed using secondary neutrons produced in a converter.

During the EURISOL_DS project the following steps have been underdone: Code validation, in-target production rates for single-stage targets and double-stage targets.

2.3.1 Code validation

Two types of experimental data have been used to validate different codes: In case of direct targets (single-stage targets), where nuclei of interest are produced via spallation reactions, residue productions have been benchmarked. On the other hand, for the fission-target case (i.e. double-stage targets) nuclei are produced by neutron-induced fission, where neutrons are created in the mercury converter via spallation-evaporation reactions. In this case neutron production is benchmarked. For benchmarking purposes MCNPX2.5.0 has been used, as it gives possibility to use 10 combinations of different intra-nuclear cascade models plus deexcitation models. Results of the benchmark on residue and neutron production from thin and thick targets have shown [47] that the most suited code combination ISABEL-ABLA or INCL4-ABLA. In case of neutron production, CEM2k could be use in cases on needs to save on the computing time. In the following, the results obtained with these code systems will be presented.

2.3.2 Production rates for single-stage targets

In order to estimate the in-target RIB production rates in direct targets 320 different configurations of cylindrical targets have been studied (more details on different target configurations can be found in Ref. [48]). Four types of material have been studied: oxides (Al_2O_3), carbides (SiC, UCx), molten metals (Pb) and refractory metals (Ta). According to the EURISOL_DS project, energy values ranging from 0.5 to 2 GeV have been selected. Finally, the power which targets have to stand up was fixed to 100 kW.

The combination of the MCNPX and CINDER codes allowed generating the list of the production rates of all nuclei. Among these rates, the production rates of eleven nuclei of interest have been specifically studied: Seven of them were given by the NUPECC board [49] (Be, Ar, Ni, Ga, Kr, Sn and Fr), and 4 additional elements which could play a pre-eminent role in the experiments planned within the EURISOL collaboration (Li, Ne, Mg and Hg) [50] have been added. Finally, for each of these elements, different isotopes of interest have been examined.

Attempting to *optimize* single-stage targets, i.e. to choose for a given nucleus the target configuration with highest production rate, according to elements or isotopes studied, one has started by plotting mass and nuclear-charge distributions for all targets and the two extreme energies. To simplify this work, radii (18 mm) and masses (2 kg) of the targets were fixed. This first study allowed reducing the number of files to be analysed, since one has obtained in this way information on which material should be used to get a given isotope of interest. A summary on the optimal target materials is given in Table 1. Note that, if Z and A numbers are not reported in Table 1, it means that two or more materials are eligible.

Table 1: Optimal target materials for the production of radioactive nuclei.

Element number	Best material	Mass number	Best material
~ 7	Al_2O_3	~ 15	Al_2O_3
~ 15	SiC	~ 30	SiC
$30 \leq Z \leq 55$	UC_3	$160 \leq A \leq 180$	Ta
$65 \leq Z \leq 70$	Ta	$185 \leq A \leq 210$	Pb
$75 \leq Z \leq 80$	Pb	≥ 215	UC_3
≥ 85	UC_3		

Concerning the 11 elements of interest, one observed that: (a) Fr nuclei can obviously only be produced using UC_3 targets, (b) Hg isotopes can essentially be produced using Pb targets, (c) Kr and Sn isotopes can essentially be produced using UC_3 targets, (d) Ar, Ni and Ga nuclei can be produced both with Pb or UC_3 targets, (e) Ne and Mg nuclei can essentially be produced using Al_2O_3 or SiC targets, (f) Li and Be isotopes can essentially be produced using Al_2O_3, SiC or UC_3 targets. Please note that this discussion is related to in-target production rates. Final intensities (and thus final choice of the target material) will be also influenced by the extraction efficiencies; this will be discussed later.

In the next step, by investigating the production rate per energy unit the optimal energy has been determined. Since the power was fixed (100 kW), the idea was that energy costs more than intensity, so for similar results one preferred those obtained with lower proton energy. Then, two-dimensional graphs – target length versus target radius – have been used in order to get optimal lengths and radii. More details can be found in [48].

2.3.3 Production rates for double-stage targets

The production rates in case of double-stage targets have been calculated in two steps: In the first step, the fission rate in the spallation neutron field has been calculated, while in the second step, the fission yields have been obtained. Six elements of interest recommended by NUPECC board were analysed in this work: Ni, Ga, Kr, Ag, Sn, Xe. In the analysis six-target assemblies configurations were accounted for: Five cases based on uranium compounds with ^{235}U percentages of 100, 20, 3, 0.72 (natural uranium) and 0.02 (depleted uranium) as well as ^{232}Th. The geometry model of the target set-up used for Monte-Carlo calculations was supplied by L. Tecchio and represents the last design variant, MAFF-like target, able to accommodate 30 kW load heat.

The present study provides quantitative estimates of the fission yields for a variety of isotopic distributions for different target systems, as shown in Figure 21.

Moreover, a comparative study between the two production scenarios used in the design – converter and direct methods – in terms of neutron and fission rate distributions and relevant fission product yields has also been carried-out [51]. In Figure 22 the two methods for producing nuclei of interest via fission are compared. Integrated yields produced via converter method are used in comparison. For the converter method the Figure 22 reveals that high intensity production yields for heavy fission fragment group enhances with the number of neutrons inside the nuclide (see upper panel of the figure) where the largest difference against the direct option reaches up to a factor 20 (for ^{140}Xe). Nuclides of the light fission fragment group are less favoured being less neutron rich (see Figure 22, bottom). As expected, a direct method is much more favourable for the production of neutron-deficient isotopes of elements considered. One can conclude that the spallation of the optimized UC_3 target by 1 GeV protons and the fission induced by low energy secondary neutrons in a ^{235}U target are complementary methods able to provide overall high intensities for secondary beams over a large domain of the chart of the nuclides.

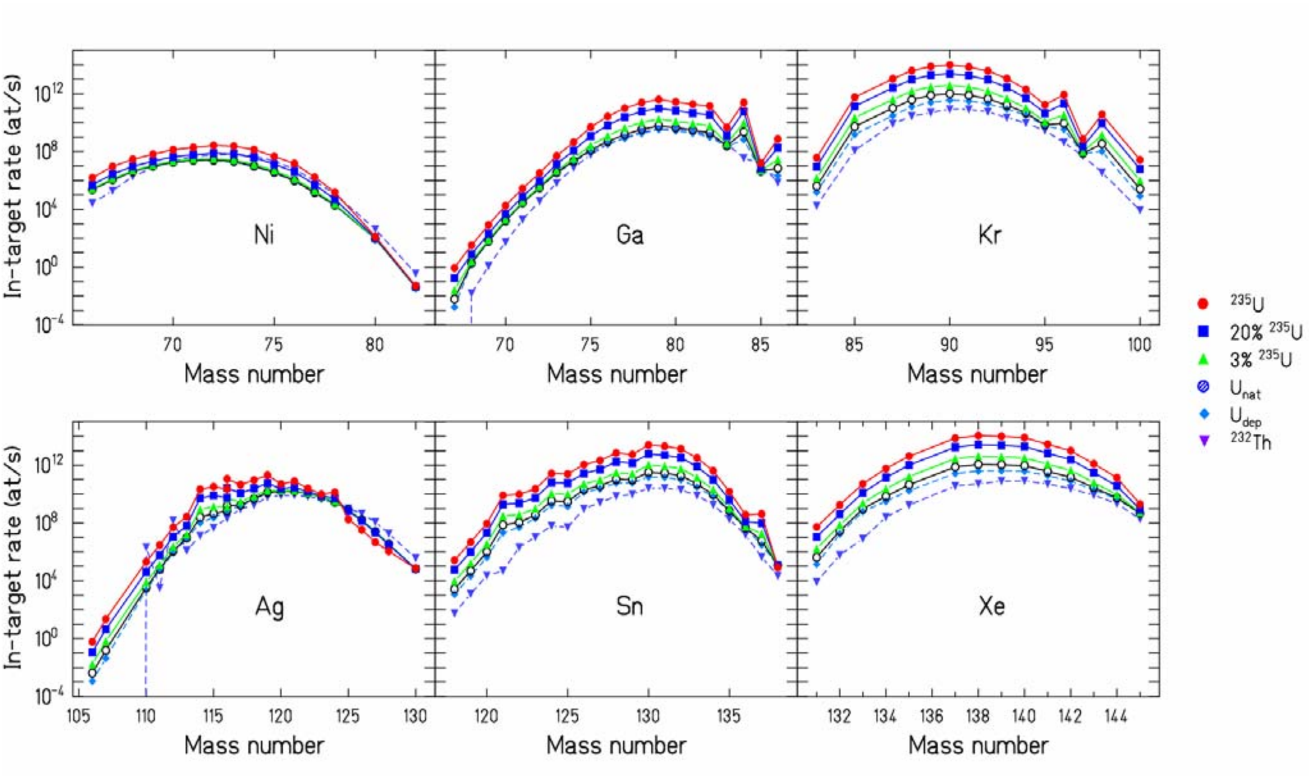

Figure 21: In-target production rates of several elements for different target configurations.

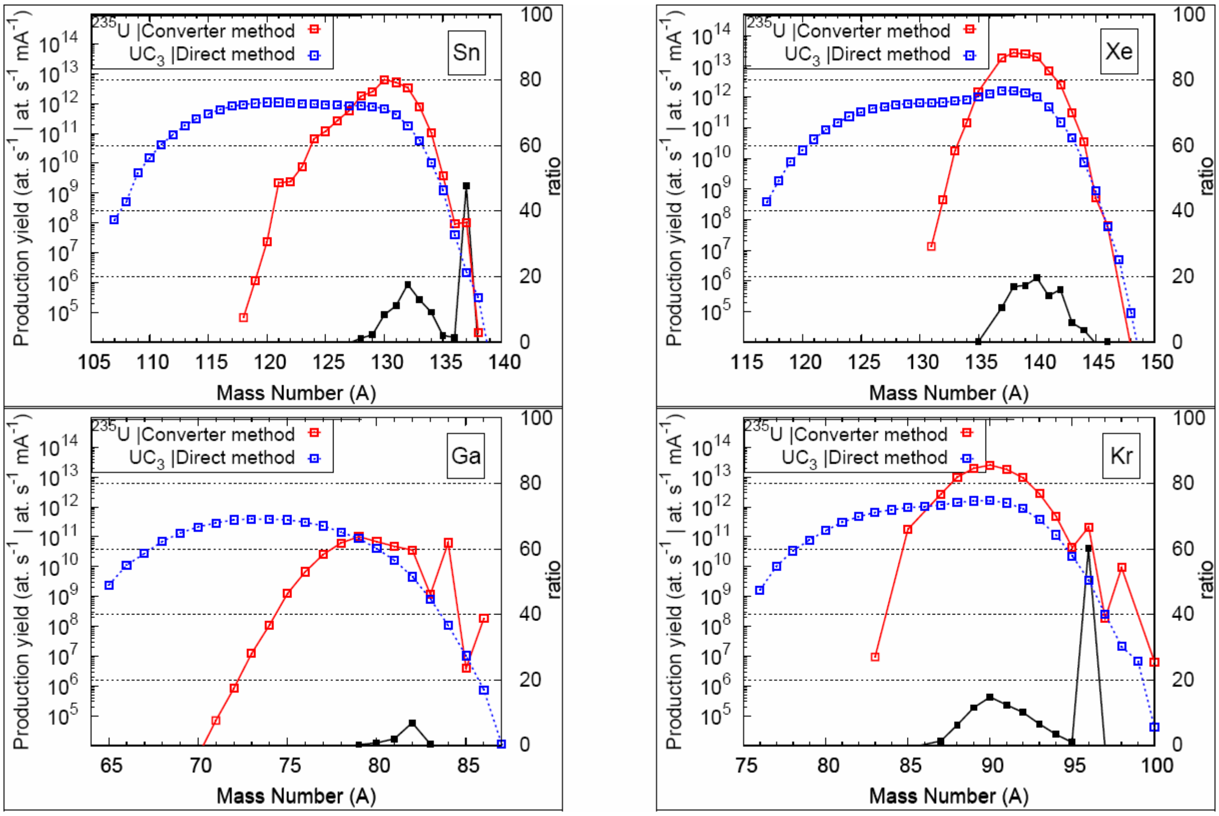

Figure 22: Comparison of the fission production yields by selected isotopes. Black curve is the ratio between converter and direct method results, scaled by the right y- axis. Only ratio values less than 100 are given in the graphs.

More details are given in [51].

3. Systematic calculations on secondary-beam intensities

The most demanding goal is to collect the available information on efficiencies for release, ionisation, transport and post acceleration for predicting most realistic secondary-beam intensities in different technical scenarios. These aspects have been studied in details in the frame of Task 3 [4], Task 4 [5] and Task 9 [6] of the EURISOL_DS Project. These must be combined with the calculated cross sections and to apply it together with the results on in-target production yields.

Information on the expected secondary-beam intensities at EURISOL will be given for the following nuclei:

- **Li, Be, Mg, Ar, Ni, Ga, Kr, Sn, Hg, Fr** (single-stage target configuration)
- **Ni, Ga, Kr, Sn** (double-stage target configuration)
- **^{131}In, ^{130}Cd, ^{129}Ag, ^{128}Pa, ^{127}Rh, $^{124\text{-}126}$Ru, $^{121\text{-}123}$Tc, $^{114\text{-}120}$Mo, $^{111\text{-}117}$Nb, $^{109\text{-}114}$Zr** (two-step option)

3.1 ISOL efficiencies and acceleration

3.1.1 ISOL efficiencies

In order to calculate secondary-beam yields, in-target production rates have to be convoluted with release and ionisation efficiencies. The calculations presented in this report, are based on efficiency information obtained from the EURISOL_R&D report [2] as well as from Refs. [52, 53]. Of course, these values have to be considered as lower values, as further improvements in target and ion-source technology will lead to increasing efficiency values.

3.1.2 Beam-preparation efficiency

Different aspect of beam preparation, e.g. mass separation, cooling and bunching, charge breeding, beam transport have been study in details in the frame of Task 9 [6]. Here, only a short summary of the input parameters needed to calculate the secondary-beam intensities at EURISOL will be given.

Concerning the beam-transport efficiency, although in practice small losses can occur, it will be assumed that it amounts to 100%. Also, the losses in the RFQ cooler and buncher will be neglected. Mass separation efficiency will also be assumed to amount to 100%, although in some cases isobaric contaminants can be several orders of magnitude more intense than the nucleus of interest. According to the present status of high-resolution mass separator design, a theoretical resolving power of 64000 is expected [54], which in the most cases is enough to perform isobaric separation. Of course, if ions of interest partially overlap by mass (within separation capability of a high-resolution separation) with isobaric contamination and one has to apply slits to reduce isobaric contamination, this could result in a reduction of intensity of wanted nucleus.

For EURISOL, it is foreseen to use ECRIS and EBIS charge breeders in parallel. This will result in several advantages [55] like e.g.: A possibility to obtain charge state comprised between A/q=2-3 and A/q=7 over the whole chart of nuclides; charge breeding efficiencies between 5-15%, with a prospect of reaching even 50% efficiency with a new EBIS configuration; charge breeding times well below one second, which are shorter than typical diffusion-effusion times from ISOL targets. Although charge-breeding efficiency depends on the nucleus considered (see e.g. [55]), in the following a charge-breeding efficiency of 10% will be assumed for all nuclei.

To conclude, in order to calculate secondary-beam intensities given in tables below, a beam-preparation efficiency of 10% has been assumed.

3.2 Single-stage target

Intensities of exotic nuclei in a single-stage target configuration have been calculated assuming 1GeV proton beam with an intensity of 100μA. As noted in Section 2.3.2 several target materials have been considered in calculating the in-target production rates. Although Ta-foil target has been proved to be the best candidate for efficient release of short-lived nuclei [56], e.g. ^{11}Li or ^{12,14}Be, studies performed in the Task 3 have shown that this target would not sustain the irradiation parameters of EURISOL [57]; therefore, Ta foil targets have not been considered in this section.

Calculated intensities are presented in Table 2. For considered nuclei, following assumptions have been made:

- Lithium isotopes – Due to the reasons mentioned above, instead of a Ta-foil target a UCx target has been assumed together with a W surface ion source. Overall extraction efficiency has been obtained by extrapolating the efficiency values for Na, K, Rb and Fr given in Ref. [52]. As discussed in Section 2.2.1, higher intensities are possible if using higher p-beam energy (2 GeV), or even better ^{3}He beam at 2 GeV.
- Beryllium isotopes – As in case of Li, UCx target instead of Ta-foil target has been assumed. Overall extraction efficiency values have been estimated by scaling down the extraction efficiency values for Ta target given in Ref. [2] by a factor 10.
- Magnesium isotopes – SiC target has been assumed. Overall extraction efficiency values have been taken from Ref. [58].
- Argon isotopes – UCx target coupled with a FEBIAD ion source has been assumed. Overall extraction efficiencies have been taken from Ref. [2].
- Nickel isotopes – UCx target coupled with a RILIS ion source has been assumed. Overall extraction efficiencies have been taken from Ref. [2]. In case of ^{56}Ni the values are given for a target with smaller dimensions (i.e. R=9mm, L=27mm).
- Gallium – UCx target coupled with a surface ionisation source has been assumed. Overall extraction efficiency values have been taken from Ref. [2].
- Krypton isotopes – As in case of Ar, UCx target and FEBIAD ion source have been assumed. Overall extraction efficiency values have been taken from Ref. [2].
- Tin isotopes – As in case of Ni, UCx target and RILIS ion source have been assumed. Overall extraction efficiency values have been taken from Ref. [2].
- Mercury isotopes – Molten Pb target coupled to a plasma ion source has been assumed. Overall extraction efficiency values have been taken from Ref. [52].
- Francium isotopes – UCx target and direct surface ionisation source have been assumed. Overall extraction efficiency values have been taken from Ref. [2].

Table 2: Calculated intensities of several secondary beams in a direct-target configuration. Efficiency values given in column 4 comprise release, ionisation and beam-preparation efficiencies. For more details, see text.

Element	**Mass number**	**In-target rate (at/s)**	**Efficiency (%)**	**Intensity (ions/s)**
Lithium (*Z*=3)	6	$4.6193 \cdot 10^{15}$	~ 6.7	~ $3.1 \cdot 10^{14}$
	7	$5.2400 \cdot 10^{15}$	~ 6.7	~ $3.5 \cdot 10^{14}$
	8	$2.6222 \cdot 10^{14}$	~ 2.1	~ $5.6 \cdot 10^{12}$
	9	$3.9107 \cdot 10^{13}$	~ 0.4	~ $1.6 \cdot 10^{11}$
	11	$1.6825 \cdot 10^{11}$	~ 0.01	~ $1.7 \cdot 10^{7}$
Beryllium (*Z*=4)	7	$4.6752 \cdot 10^{14}$	~ $8.0 \cdot 10^{-2}$	~ $3.8 \cdot 10^{11}$
	9	$3.0224 \cdot 10^{14}$	~ $8.0 \cdot 10^{-2}$	~ $2.4 \cdot 10^{11}$
	10	$7.4529 \cdot 10^{13}$	~ $8.0 \cdot 10^{-2}$	~ $6.0 \cdot 10^{10}$
	11	$5.6233 \cdot 10^{11}$	~ 6.5-10-2	~ $3.7 \cdot 10^{8}$
	12	$1.2301 \cdot 10^{10}$	~ $5.8 \cdot 10^{-4}$	~ $7.1 \cdot 10^{4}$

Magnesium (Z=12)	22	$6.50813\cdot10^{11}$	$\sim 2.8\cdot10^{-5}$	$\sim 1.8\cdot10^{5}$
	23	$6.48781\cdot10^{12}$	$\sim 1.4\cdot10^{-4}$	$\sim 9.1\cdot10^{6}$
Argon (Z=18)	36	$6.2483\cdot10^{8}$	9.6	$6.0\cdot10^{7}$
	37	$1.9995\cdot10^{9}$	9.6	$1.9\cdot10^{8}$
	38	$4.3740\cdot10^{9}$	9.6	$4.2\cdot10^{8}$
	39	$7.2482\cdot10^{9}$	9.6	$7.0\cdot10^{8}$
	40	$9.7476\cdot10^{9}$	9.6	$9.4\cdot10^{8}$
	41	$9.7476\cdot10^{9}$	9.7	$9.4\cdot10^{8}$
	42	$1.1247\cdot10^{10}$	9.6	$1.1\cdot10^{9}$
	43	$7.2482\cdot10^{9}$	9.6	$7.0\cdot10^{8}$
	44	$3.6241\cdot10^{9}$	9.4	$3.4\cdot10^{8}$
	45	$1.6246\cdot10^{9}$	8.2	$1.3\cdot10^{8}$
	46	$7.4976\cdot10^{8}$	7.8	$5.8\cdot10^{7}$
Nickel (Z=28)	_56*_	$\mathit{1.2500\cdot10^{8}}$	5.0	$\mathit{6.3\cdot10^{6}}$
	59	$5.1236\cdot10^{9}$	5.0	$2.6\cdot10^{8}$
	63	$1.1910\cdot10^{11}$	5.0	$5.9\cdot10^{9}$
	65	$1.9249\cdot10^{11}$	4.8	$9.3\cdot10^{9}$
	66	$2.0358\cdot10^{11}$	4.9	$9.9\cdot10^{9}$
	67	$1.8838\cdot10^{11}$	0.8	$1.6\cdot10^{9}$
	68	$1.3915\cdot10^{11}$	1.1	$1.5\cdot10^{9}$
	69	$9.7409\cdot10^{10}$	0.5	$4.5\cdot10^{8}$
	70	$5.1330\cdot10^{10}$	0.2	$1.3\cdot10^{8}$
	71	$2.1239\cdot10^{10}$	0.1	$2.0\cdot10^{7}$
	72	$1.0364\cdot10^{10}$	0.05	$5.0\cdot10^{6}$
	73	$2.7171\cdot10^{9}$	0.02	$4.5\cdot10^{5}$
	74	$7.9328\cdot10^{8}$	0.02	$1.7\cdot10^{5}$
	75	$1.4188\cdot10^{8}$	0.004	$5.3\cdot10^{3}$
	76	$4.2201\cdot10^{6}$	0.002	$9.7\cdot10^{1}$
	77	$6.1530\cdot10^{5}$	0.001	5.1
Gallium (Z=31)	65	$2.3744\cdot10^{9}$	5.0	$1.2\cdot10^{8}$
	66	$1.1123\cdot10^{10}$	5.0	$5.6\cdot10^{8}$
	67	$2.7618\cdot10^{10}$	5.0	$1.4\cdot10^{9}$
	68	$6.9983\cdot10^{10}$	5.0	$3.5\cdot10^{9}$
	70	$2.1445\cdot10^{11}$	5.0	$1.1\cdot10^{10}$
	72	$3.7192\cdot10^{11}$	5.0	$1.9\cdot10^{10}$
	73	$3.9216\cdot10^{11}$	5.0	$2.0\cdot10^{10}$
	74	$3.8626\cdot10^{11}$	5.0	$1.9\cdot10^{10}$
	75	$3.6735\cdot10^{11}$	5.0	$1.8\cdot10^{10}$
	76	$3.0431\cdot10^{11}$	4.6	$1.4\cdot10^{10}$
	77	$2.3122\cdot10^{11}$	4.6	$1.1\cdot10^{10}$
	78	$1.4261\cdot10^{11}$	3.9	$5.6\cdot10^{9}$
	79	$8.6795\cdot10^{10}$	3.4	$3.0\cdot10^{9}$
	80	$4.0484\cdot10^{10}$	2.9	$1.2\cdot10^{9}$
	81	$1.6107\cdot10^{10}$	2.8	$4.5\cdot10^{8}$
	82	$4.5603\cdot10^{9}$	2.4	$1.1\cdot10^{8}$
	83	$8.2616\cdot10^{8}$	2.1	$1.7\cdot10^{7}$
	84	$1.0644\cdot10^{8}$	1.6	$1.7\cdot10^{6}$
Krypton (Z=36)	76	$1.6246\cdot10^{9}$	9.2	$1.5\cdot10^{8}$
	77	$1.0248\cdot10^{10}$	9.2	$9.4\cdot10^{8}$
	79	$7.6856\cdot10^{10}$	9.2	$7.1\cdot10^{9}$

	81	$3.0631\cdot10^{11}$	9.2	$2.8\cdot10^{10}$
	85	$9.5316\cdot10^{11}$	9.2	$8.8\cdot10^{10}$
	87	$1.1631\cdot10^{12}$	9.1	$1.1\cdot10^{11}$
	88	$1.3926\cdot10^{12}$	9.2	$1.3\cdot10^{11}$
	89	$1.5945\cdot10^{12}$	8.9	$1.4\cdot10^{11}$
	90	$1.6259\cdot10^{12}$	8.5	$1.4\cdot10^{11}$
	91	$1.3777\cdot10^{12}$	7.3	$1.0\cdot10^{11}$
	92	$8.6970\cdot10^{11}$	4.6	$4.0\cdot10^{10}$
	93	$3.7242\cdot10^{11}$	3.7	$1.4\cdot10^{10}$
	94	$1.1561\cdot10^{11}$	1.0	$1.1\cdot10^{9}$
	95	$2.2802\cdot10^{10}$	0.5	$1.2\cdot10^{8}$
	96	$3.5266\cdot10^{9}$	0.5	$1.9\cdot10^{7}$
	97	$2.5301\cdot10^{8}$	0.6	$1.5\cdot10^{6}$
	98	$2.0804\cdot10^{7}$	0.4	$8.7\cdot10^{4}$
	99	$6.6442\cdot10^{6}$	0.3	$2.1\cdot10^{4}$
	100	$4.0680\cdot10^{4}$	0.2	$8.1\cdot10^{1}$
Tin (Z=50)	107	$1.2497\cdot10^{8}$	4.7	$5.9\cdot10^{6}$
	108	$4.9989\cdot10^{8}$	5.0	$2.5\cdot10^{7}$
	109	$4.7489\cdot10^{9}$	5.0	$2.4\cdot10^{8}$
	110	$1.4996\cdot10^{10}$	5.0	$7.5\cdot10^{8}$
	111	$4.2487\cdot10^{10}$	5.0	$2.1\cdot10^{9}$
	113	$1.8321\cdot10^{11}$	5.0	$9.2\cdot10^{9}$
	121	$1.1009\cdot10^{12}$	5.0	$5.5\cdot10^{10}$
	123	$1.0027\cdot10^{12}$	5.0	$5.0\cdot10^{10}$
	125	$9.2384\cdot10^{11}$	5.0	$4.6\cdot10^{10}$
	126	$8.7971\cdot10^{11}$	5.0	$4.4\cdot10^{10}$
	127	$8.5348\cdot10^{11}$	5.0	$4.3\cdot10^{10}$
	128	$8.4531\cdot10^{11}$	2.4	$2.1\cdot10^{10}$
	129	$7.8549\cdot10^{11}$	4.6	$3.6\cdot10^{10}$
	130	$6.8104\cdot10^{11}$	4.8	$3.3\cdot10^{10}$
	131	$4.2982\cdot10^{11}$	4.4	$1.9\cdot10^{10}$
	132	$1.8319\cdot10^{11}$	4.2	$7.6\cdot10^{9}$
	133	$5.7469\cdot10^{10}$	0.9	$5.1\cdot10^{8}$
	134	$1.0199\cdot10^{10}$	0.7	$7.1\cdot10^{7}$
Mercury (Z=80)	178	$3.7437\cdot10^{8}$	0.0001	$2.9\cdot10^{2}$
	179	$2.7484\cdot10^{9}$	0.001	$3.2\cdot10^{4}$
	180	$1.3620\cdot10^{10}$	0.006	$8.4\cdot10^{5}$
	181	$4.6483\cdot10^{10}$	0.01	$5.5\cdot10^{6}$
	182	$1.4808\cdot10^{11}$	0.09	$1.3\cdot10^{8}$
	183	$3.5427\cdot10^{11}$	0.07	$2.5\cdot10^{8}$
	184	$6.7996\cdot10^{11}$	0.4	$2.6\cdot10^{9}$
	185	$1.1598\cdot10^{12}$	0.6	$6.4\cdot10^{9}$
	186	$1.7554\cdot10^{12}$	0.7	$1.2\cdot10^{10}$
	187	$2.3772\cdot10^{12}$	0.7	$1.8\cdot10^{10}$
	188	$3.0034\cdot10^{12}$	0.8	$2.3\cdot10^{10}$
	189	$3.5295\cdot10^{12}$	0.8	$2.7\cdot10^{10}$
	190	$3.9600\cdot10^{12}$	0.8	$3.1\cdot10^{10}$
	191	$4.2546\cdot10^{12}$	0.8	$3.3\cdot10^{10}$
	192	$4.2841\cdot10^{12}$	0.8	$3.3\cdot10^{10}$
	193	$4.3153\cdot10^{12}$	0.8	$3.4\cdot10^{10}$
	194	$4.1737\cdot10^{12}$	0.8	$3.3\cdot10^{10}$

	195	$4.0548\cdot10^{12}$	0.8	$3.2\cdot10^{10}$
	197	$3.5873\cdot10^{12}$	0.8	$2.8\cdot10^{10}$
	203	$1.8246\cdot10^{12}$	0.8	$1.4\cdot10^{10}$
	205	$1.2740\cdot10^{12}$	0.8	$9.8\cdot10^{9}$
	206	$4.7290\cdot10^{11}$	0.8	$3.7\cdot10^{9}$
	207	$7.4233\cdot10^{10}$	0.8	$5.6\cdot10^{8}$
	208	$1.2497\cdot10^{8}$	0.8	$9.8\cdot10^{5}$
Francium (Z=87)	203	$1.2488\cdot10^{8}$	0.9	$1.2\cdot10^{6}$
	204	$4.9978\cdot10^{8}$	2.0	$9.8\cdot10^{6}$
	205	$1.7494\cdot10^{9}$	2.6	$4.5\cdot10^{7}$
	206	$3.4992\cdot10^{9}$	3.9	$1.4\cdot10^{8}$
	207	$1.1622\cdot10^{10}$	3.8	$4.4\cdot10^{8}$
	208	$2.0620\cdot10^{10}$	4.8	$9.8\cdot10^{8}$
	209	$4.8114\cdot10^{10}$	4.5	$2.2\cdot10^{9}$
	210	$7.3356\cdot10^{10}$	4.9	$3.6\cdot10^{9}$
	211	$1.1724\cdot10^{11}$	4.8	$5.7\cdot10^{9}$
	212	$1.5823\cdot10^{11}$	4.9	$7.7\cdot10^{9}$
	213	$2.0307\cdot10^{11}$	4.3	$8.8\cdot10^{9}$
	219	$1.0272\cdot10^{11}$	0.2	$2.0\cdot10^{8}$
	220	$7.4610\cdot10^{10}$	4.2	$3.1\cdot10^{9}$
	221	$6.2110\cdot10^{10}$	4.9	$3.0\cdot10^{9}$
	222	$5.0861\cdot10^{10}$	4.9	$2.5\cdot10^{9}$
	223	$3.2742\cdot10^{10}$	4.8	$1.6\cdot10^{9}$
	224	$2.5244\cdot10^{10}$	4.8	$1.2\cdot10^{9}$
	225	$1.4247\cdot10^{10}$	4.9	$7.0\cdot10^{8}$
	226	$1.1872\cdot10^{10}$	4.5	$5.3\cdot10^{8}$
	227	$6.9986\cdot10^{9}$	4.9	$3.4\cdot10^{8}$
	228	$5.1239\cdot10^{9}$	4.3	$2.2\cdot10^{8}$
	229	$4.4989\cdot10^{9}$	4.6	$2.1\cdot10^{8}$
	230	$2.8743\cdot10^{9}$	4.1	$1.2\cdot10^{8}$
	231	$1.7495\cdot10^{9}$	4.6	$8.1\cdot10^{7}$

** Comment on ^{56}Ni production – see text.*

3.3 Double-stage target

Secondary-beam intensities in a double-stage target configuration have been calculated for five different target materials. They are listed in Table 3 together with calculated fission rates for each case.

Table 3: Calculated fission rates for different fission-target materials.

Target material	**Fission rate (fissions/s/mA)**
^{235}U	$5.7689\cdot10^{14}$
20% ^{235}U	$1.3943\cdot10^{14}$
3% ^{235}U	$2.3106\cdot10^{13}$
U_{nat}	$6.6621\cdot10^{12}$
U_{dep}	$2.8814\cdot10^{12}$

In Table 4-Table ***8*** are given calculated intensities of several chosen elements (Ni, Ga, Kr and Sn). These calculations are based on the in-target yields presented in Section 2.3.3 (and given in the third column of Table 4-Table ***8***) and on release, ionisation and beam-preparation efficiencies presented in Section 3.1 (total efficiencies are given in the fourth column of Table 4-Table ***8***). Except for Kr, for all other nuclei considered, a RILIS ion source is assumed, and expected gains in ionisation efficiency as given in the EURISOL_R&D report (see Table 2.2 from Ref. [49]) have been taken into account. In case of Kr, FEBIAD ion source is assumed (as in [49]), with an average gain in ionisation efficiency of a factor 20. For ^{80}Ni, ^{100}Kr and ^{138}Sn half-lives of 35 ms, 30 ms and 60 ms, respectively, have been assumed.

Table 4: Calculated intensities of several secondary beams in case of pure ^{235}U target. Efficiency values given in column 4 comprise release, ionisation and beam-preparation efficiencies.

Element	**Mass number**	**In-target rate (at/s)**	**Efficiency (%)**	**Intensity (ions/s)**
Nickel (*Z*=28)	66	$1.5689 \cdot 10^{6}$	< 63.8	$< 1.0 \cdot 10^{6}$
	67	$9.3977 \cdot 10^{6}$	< 14.2	$< 1.3 \cdot 10^{6}$
	68	$2.8991 \cdot 10^{7}$	< 17.4	$< 5.0 \cdot 10^{6}$
	69	$6.4432 \cdot 10^{7}$	7.7	$4.9 \cdot 10^{6}$
	70	$1.3368 \cdot 10^{8}$	4.0	$5.4 \cdot 10^{6}$
	71	$1.8863 \cdot 10^{8}$	1.5	$2.9 \cdot 10^{6}$
	72	$2.6303 \cdot 10^{8}$	0.8	$2.1 \cdot 10^{6}$
	73	$2.335 \cdot 10^{8}$	0.35	$8.1 \cdot 10^{5}$
	74	$1.3662 \cdot 10^{8}$	0.35	$4.8 \cdot 10^{5}$
	75	$4.5994 \cdot 10^{7}$	0.083	$3.8 \cdot 10^{4}$
	76	$1.4919 \cdot 10^{7}$	0.047	$7.0 \cdot 10^{3}$
	77	$1.7288 \cdot 10^{6}$	0.037	$6.5 \cdot 10^{2}$
	78	$1.5181 \cdot 10^{5}$	0.032	$4.8 \cdot 10^{1}$
	80	$1.3378 \cdot 10^{2}$	0.008	1.1
Gallium (*Z*=31)	68	$3.31 \cdot 10^{1}$	5.0	1.7
	69	$8.33 \cdot 10^{2}$	5.0	$4.2 \cdot 10^{1}$
	70	$1.82 \cdot 10^{4}$	5.0	$9.1 \cdot 10^{2}$
	71	$2.767 \cdot 10^{5}$	5.0	$1.4 \cdot 10^{4}$
	72	$3.297 \cdot 10^{6}$	5.0	$1.6 \cdot 10^{5}$
	73	$4.894 \cdot 10^{7}$	5.0	$2.4 \cdot 10^{6}$
	74	$4.412 \cdot 10^{8}$	5.0	$2.2 \cdot 10^{7}$
	75	$4.923 \cdot 10^{9}$	4.9	$2.4 \cdot 10^{8}$
	76	$2.67 \cdot 10^{10}$	4.9	$1.3 \cdot 10^{9}$
	77	$1.014 \cdot 10^{11}$	4.5	$4.6 \cdot 10^{9}$
	78	$2.467 \cdot 10^{11}$	4.0	$1.0 \cdot 10^{10}$

	79	$4.028\cdot10^{11}$	3.5	$1.4\cdot10^{10}$
	80	$2.753\cdot10^{11}$	3.0	$8.2\cdot10^{9}$
	81	$1.898\cdot10^{11}$	2.6	$5.0\cdot10^{9}$
	82	$1.425\cdot10^{11}$	1.8	$2.5\cdot10^{9}$
	83	$4.649\cdot10^{9}$	1.1	$5.1\cdot10^{7}$
	84	$2.501\cdot10^{11}$	0.3	$8.3\cdot10^{8}$
	85	$1.549\cdot10^{7}$	0.2	$2.9\cdot10^{4}$
	86	$7.389\cdot10^{8}$	0.1	$7.7\cdot10^{5}$
Krypton (Z=36)	83m ($t_{1/2}$ = 1.83 h)	$3.7133\cdot10^{7}$	8.8	$3.3\cdot10^{6}$
	85m ($t_{1/2}$ = 4.48 h)	$1.3314\cdot10^{7}$	8.8	$1.2\cdot10^{6}$
	85	$5.7722\cdot10^{11}$	8.8	$5.1\cdot10^{10}$
	87	$1.0628\cdot10^{13}$	9.2	$9.7\cdot10^{11}$
	88	$3.9614\cdot10^{13}$	8.8	$3.5\cdot10^{12}$
	89	$7.8789\cdot10^{13}$	8.5	$6.7\cdot10^{12}$
	90	$1.011\cdot10^{14}$	8.4	$8.6\cdot10^{12}$
	91	$7.2616\cdot10^{13}$	7.0	$5.1\cdot10^{12}$
	92	$3.8059\cdot10^{13}$	4.9	$1.9\cdot10^{12}$
	93	$1.1099\cdot10^{13}$	4.4	$4.9\cdot10^{11}$
	94	$1.9876\cdot10^{12}$	1.3	$2.7\cdot10^{10}$
	95	$1.7300\cdot10^{11}$	0.7	$1.2\cdot10^{9}$
	96	$8.5263\cdot10^{11}$	0.6	$5.5\cdot10^{9}$
	97	$7.2753\cdot10^{8}$	0.5	$3.9\cdot10^{6}$
	98	$3.6721\cdot10^{10}$	0.4	$1.4\cdot10^{8}$
	100	$2.5906\cdot10^{7}$	0.2	$6.2\cdot10^{4}$
Tin (Z=50)	118	$2.691\cdot10^{5}$	5.0	$1.3\cdot10^{4}$
	119	$4.677\cdot10^{6}$	5.0	$2.3\cdot10^{5}$
	121m ($t_{1/2}$ = 55 y)	$7.867\cdot10^{8}$	5.0	$3.9\cdot10^{7}$
	121	$8.104\cdot10^{9}$	5.0	$4.1\cdot10^{8}$
	123m ($t_{1/2}$ = 40.06 min)	$8.229\cdot10^{9}$	5.0	$4.1\cdot10^{8}$
	123	$2.27\cdot10^{10}$	5.0	$1.1\cdot10^{9}$
	125m ($t_{1/2}$ = 9.52 min)	$2.441\cdot10^{11}$	5.0	$1.2\cdot10^{10}$
	125	$2.276\cdot10^{11}$	4.9	$1.1\cdot10^{10}$
	126	$1.080\cdot10^{12}$	5.0	$5.4\cdot10^{10}$
	127m ($t_{1/2}$ = 4.13 min)	$2.181\cdot10^{11}$	5.0	$1.1\cdot10^{10}$
	127	$2.085\cdot10^{12}$	4.8	$1.0\cdot10^{11}$

	128	$7.059 \cdot 10^{12}$	2.4	$1.7 \cdot 10^{11}$
	129m ($t_{1/2}$ = 6.9 min)	$4.516 \cdot 10^{12}$	5.0	$2.3 \cdot 10^{11}$
	129	$5.493 \cdot 10^{12}$	4.6	$2.5 \cdot 10^{11}$
	130	$2.498 \cdot 10^{13}$	5.0	$1.2 \cdot 10^{12}$
	131	$2.051 \cdot 10^{13}$	4.4	$9.0 \cdot 10^{11}$
	132	$1.349 \cdot 10^{13}$	4.2	$5.6 \cdot 10^{11}$
	133	$3.173 \cdot 10^{12}$	0.9	$2.7 \cdot 10^{10}$
	134	$4.065 \cdot 10^{11}$	0.7	$2.9 \cdot 10^{9}$
	135	$1.488 \cdot 10^{10}$	0.3	$5.0 \cdot 10^{7}$
	136	$3.691 \cdot 10^{8}$	0.2	$5.5 \cdot 10^{5}$
	137	$4.192 \cdot 10^{8}$	0.1	$4.5 \cdot 10^{5}$
	138	$8.274 \cdot 10^{4}$	0.05	$3.8 \cdot 10^{1}$

Table 5: Calculated intensities of several secondary beams in case of uranium target containing 20% ^{235}U. Efficiency values given in column 4 comprise release, ionisation and beam-preparation efficiencies.

Element	**Mass number**	**In-target rate (at/s)**	**Efficiency (%)**	**Intensity (ions/s)**
Nickel (*Z*=28)	66	$4.9361 \cdot 10^{5}$	< 63.8	$< 3.2 \cdot 10^{5}$
	67	$2.7763 \cdot 10^{6}$	< 14.2	$< 3.9 \cdot 10^{5}$
	68	$9.4406 \cdot 10^{6}$	< 17.4	$< 1.6 \cdot 10^{6}$
	69	$2.1480 \cdot 10^{7}$	7.7	$1.6 \cdot 10^{6}$
	70	$4.3201 \cdot 10^{7}$	4.0	$1.7 \cdot 10^{6}$
	71	$6.0368 \cdot 10^{7}$	1.5	$9.3 \cdot 10^{5}$
	72	$7.7720 \cdot 10^{7}$	0.8	$6.2 \cdot 10^{5}$
	73	$6.8291 \cdot 10^{7}$	0.35	$2.4 \cdot 10^{5}$
	74	$3.8481 \cdot 10^{7}$	0.35	$1.4 \cdot 10^{5}$
	75	$1.3318 \cdot 10^{7}$	0.083	$1.1 \cdot 10^{4}$
	76	$4.1069 \cdot 10^{6}$	0.047	$1.9 \cdot 10^{3}$
	77	$5.0424 \cdot 10^{5}$	0.037	$1.9 \cdot 10^{2}$
	78	$5.0392 \cdot 10^{4}$	0.032	$1.6 \cdot 10^{1}$
	80	$1.0498 \cdot 10^{2}$	0.008	0.8
Gallium (*Z*=31)	68	$2.097 \cdot 10^{2}$	5.0	$3.9 \cdot 10^{-1}$
	69	$4.737 \cdot 10^{3}$	5.0	$1.0 \cdot 10^{1}$
	70	$7.655 \cdot 10^{4}$	5.0	$2.4 \cdot 10^{2}$
	71	$9.161 \cdot 10^{5}$	5.0	$3.8 \cdot 10^{3}$
	72	$1.339 \cdot 10^{7}$	5.0	$4.6 \cdot 10^{4}$

	73	$1.160\cdot10^{8}$	5.0	$6.7\cdot10^{5}$
	74	$1.227\cdot10^{9}$	5.0	$5.8\cdot10^{6}$
	75	$6.494\cdot10^{9}$	4.9	$6.1\cdot10^{7}$
	76	$2.441\cdot10^{10}$	4.9	$3.2\cdot10^{8}$
	77	$5.966\cdot10^{10}$	4.5	$1.1\cdot10^{9}$
	78	$9.807\cdot10^{10}$	4.0	$2.4\cdot10^{9}$
	79	$6.742\cdot10^{10}$	3.5	$3.5\cdot10^{9}$
	80	$4.662\cdot10^{10}$	3.0	$2.0\cdot10^{9}$
	81	$3.480\cdot10^{10}$	2.6	$1.2\cdot10^{9}$
	82	$1.278\cdot10^{9}$	1.8	$6.1\cdot10^{8}$
	83	$6.024\cdot10^{10}$	1.1	$1.4\cdot10^{7}$
	84	$7.319\cdot10^{6}$	0.3	$2.0\cdot10^{8}$
	85	$1.781\cdot10^{8}$	0.2	$1.4\cdot10^{4}$
	86	$2.097\cdot10^{2}$	0.1	$1.9\cdot10^{5}$
Krypton (Z=36)	83m ($t_{1/2}$ = 1.83 h)	$8.8863\cdot10^{6}$	8.8	$7.8\cdot10^{5}$
	85m ($t_{1/2}$ = 4.48 h)	$3.2044\cdot10^{10}$	8.8	$2.8\cdot10^{9}$
	85	$1.3892\cdot10^{11}$	8.8	$1.2\cdot10^{10}$
	87	$2.5517\cdot10^{12}$	9.2	$2.3\cdot10^{11}$
	88	$9.5270\cdot10^{12}$	8.8	$8.4\cdot10^{11}$
	89	$1.8949\cdot10^{13}$	8.5	$1.6\cdot10^{12}$
	90	$2.4327\cdot10^{13}$	8.4	$2.1\cdot10^{12}$
	91	$1.7520\cdot10^{13}$	7.0	$1.2\cdot10^{12}$
	92	$9.2245\cdot10^{12}$	4.9	$4.5\cdot10^{11}$
	93	$2.7142\cdot10^{12}$	4.4	$1.2\cdot10^{11}$
	94	$5.0157\cdot10^{11}$	1.3	$6.7\cdot10^{9}$
	95	$4.5752\cdot10^{10}$	0.7	$3.\ 1\cdot10^{8}$
	96	$2.0635\cdot10^{11}$	0.6	$1.3\cdot10^{9}$
	97	$2.2899\cdot10^{8}$	0.5	$1.2\cdot10^{6}$
	98	$8.8493\cdot10^{9}$	0.4	$3.4\cdot10^{7}$
	100	$6.2510\cdot10^{6}$	0.2	$1.5\cdot10^{4}$
Tin (Z=50)	118	$5.710\cdot10^{4}$	5.0	$2.9\cdot10^{3}$
	119	$1.037\cdot10^{6}$	5.0	$5.2\cdot10^{4}$
	121m ($t_{1/2}$ = 55 y)	$1.838\cdot10^{8}$	5.0	$9.2\cdot10^{6}$
	121	$1.950\cdot10^{9}$	5.0	$9.8\cdot10^{7}$
	123m ($t_{1/2}$ = 40.06 min)	$1.949\cdot10^{9}$	5.0	$9.7\cdot10^{7}$
	123	$5.372\cdot10^{9}$	5.0	$2.7\cdot10^{8}$
	125m ($t_{1/2}$ = 9.52 min)	$5.902\cdot10^{10}$	5.0	$3.0\cdot10^{9}$

	125	$5.588\cdot10^{10}$	4.9	$2.8\cdot10^{9}$
	126	$2.652\cdot10^{11}$	5.0	$1.3\cdot10^{10}$
	127m ($t_{1/2}$ = 4.13 min)	$5.397\cdot10^{10}$	5.0	$2.7\cdot10^{9}$
	127	$5.109\cdot10^{11}$	4.8	$2.4\cdot10^{10}$
	128	$1.719\cdot10^{12}$	2.4	$4.2\cdot10^{10}$
	129m ($t_{1/2}$ = 6.9 min)	$1.093\cdot10^{12}$	5.0	$5.5\cdot10^{10}$
	129	$1.346\cdot10^{12}$	4.6	$6.2\cdot10^{10}$
	130	$6.057\cdot10^{12}$	5.0	$3.0\cdot10^{11}$
	131	$4.983\cdot10^{12}$	4.4	$2.2\cdot10^{11}$
	132	$3.294\cdot10^{12}$	4.2	$1.4\cdot10^{11}$
	133	$7.798\cdot10^{11}$	0.9	$6.7\cdot10^{9}$
	134	$1.022\cdot10^{11}$	0.7	$7.4\cdot10^{8}$
	135	$4.034\cdot10^{9}$	0.3	$1.3\cdot10^{7}$
	136	$1.250\cdot10^{8}$	0.2	$1.9\cdot10^{5}$
	137	$1.026\cdot10^{8}$	0.1	$1.1\cdot10^{5}$
	138	$1.179\cdot10^{5}$	0.05	$5.4\cdot10^{1}$

Table 6: Calculated intensities of several secondary beams in case of uranium target containing 3% ^{235}U. Efficiency values given in column 4 comprise release, ionisation and beam-preparation efficiencies.

Element	**Mass number**	**In-target rate (at/s)**	**Efficiency (%)**	**Intensity (ions/s)**
Nickel (Z=28)	66	$2.6280\cdot10^{5}$	< 63.8	< $1.7\cdot10^{5}$
	67	$1.3014\cdot10^{6}$	< 14.2	< $1.8\cdot10^{5}$
	68	$4.9079\cdot10^{6}$	< 17.4	< $8.5\cdot10^{5}$
	69	$1.1305\cdot10^{7}$	7.7	$8.7\cdot10^{5}$
	70	$2.1379\cdot10^{7}$	4.0	$8.6\cdot10^{5}$
	71	$2.9051\cdot10^{7}$	1.5	$4.5\cdot10^{5}$
	72	$3.1342\cdot10^{7}$	0.8	$2.5\cdot10^{5}$
	73	$2.6600\cdot10^{7}$	0.35	$9.3\cdot10^{4}$
	74	$1.3370\cdot10^{7}$	0.35	$4.7\cdot10^{4}$
	75	$4.9453\cdot10^{6}$	0.083	$4.1\cdot10^{3}$
	76	$1.3498\cdot10^{6}$	0.047	$6.4\cdot10^{2}$
	77	$1.9102\cdot10^{5}$	0.037	$7.1\cdot10^{1}$
	78	$2.3787\cdot10^{4}$	0.032	7.5
	80	$9.5207\cdot10^{1}$	0.008	0.8
Gallium (Z=31)	68	2.555	5.0	$1.3\cdot10^{-1}$
	69	$8.065\cdot10^{1}$	5.0	4.0

	70	$1.929\cdot10^{3}$	5.0	$9.6\cdot10^{1}$
	71	$3.399\cdot10^{4}$	5.0	$1.7\cdot10^{3}$
	72	$3.815\cdot10^{5}$	5.0	$1.9\cdot10^{4}$
	73	$4.770\cdot10^{6}$	5.0	$2.4\cdot10^{5}$
	74	$3.355\cdot10^{7}$	5.0	$1.7\cdot10^{6}$
	75	$2.629\cdot10^{8}$	4.9	$1.3\cdot10^{7}$
	76	$1.240\cdot10^{9}$	4.9	$6.0\cdot10^{7}$
	77	$4.314\cdot10^{9}$	4.5	$2.0\cdot10^{8}$
	78	$1.039\cdot10^{10}$	4.0	$4.2\cdot10^{8}$
	79	$1.742\cdot10^{10}$	3.5	$6.2\cdot10^{8}$
	80	$1.234\cdot10^{10}$	3.0	$3.7\cdot10^{8}$
	81	$8.545\cdot10^{9}$	2.6	$2.3\cdot10^{8}$
	82	$6.036\cdot10^{9}$	1.8	$1.1\cdot10^{8}$
	83	$3.752\cdot10^{8}$	1.1	$4.1\cdot10^{6}$
	84	$9.507\cdot10^{9}$	0.3	$3.2\cdot10^{7}$
	85	$4.829\cdot10^{6}$	0.2	$9.1\cdot10^{3}$
	86	$2.825\cdot10^{7}$	0.1	$2.9\cdot10^{4}$
Krypton (Z=36)	83m ($t_{1/2}$= 1.83 h)	$1.4463\cdot10^{6}$	8.8	$1.3\cdot10^{5}$
	85m ($t_{1/2}$= 4.48 h)	$5.0494\cdot10^{9}$	8.8	$4.4\cdot10^{8}$
	85	$2.1931\cdot10^{10}$	8.8	$1.9\cdot10^{9}$
	87	$4.0383\cdot10^{11}$	9.2	$3.7\cdot10^{10}$
	88	$1.5197\cdot10^{12}$	8.8	$1.3\cdot10^{11}$
	89	$3.0249\cdot10^{12}$	8.5	$2.6\cdot10^{11}$
	90	$3.9115\cdot10^{12}$	8.4	$3.3\cdot10^{11}$
	91	$2.8642\cdot10^{12}$	7.0	$2.0\cdot10^{11}$
	92	$1.5445\cdot10^{12}$	4.9	$7.6\cdot10^{10}$
	93	$4.7611\cdot10^{11}$	4.4	$2.1\cdot10^{10}$
	94	$1.0328\cdot10^{11}$	1.3	$1.4\cdot10^{9}$
	95	$1.1814\cdot10^{10}$	0.7	$7.9\cdot10^{7}$
	96	$3.3566\cdot10^{10}$	0.6	$2.1\cdot10^{8}$
	97	$9.3320\cdot10^{7}$	0.5	$4.9\cdot10^{5}$
	98	$1.4002\cdot10^{9}$	0.4	$5.3\cdot10^{6}$
	100	$9.9713\cdot10^{5}$	0.2	$2.4\cdot10^{3}$
Tin (Z=50)	118	$9.209\cdot10^{3}$	5.0	$4.6\cdot10^{2}$
	119	$1.685\cdot10^{5}$	5.0	$8.4\cdot10^{3}$
	121m ($t_{1/2}$= 55 y)	$3.058\cdot10^{7}$	5.0	$1.5\cdot10^{6}$
	121	$3.069\cdot10^{8}$	5.0	$1.5\cdot10^{7}$

	123m ($t_{1/2}$ = 40.06 min)	$3.345\cdot10^{8}$	5.0	$1.7\cdot10^{7}$
	123	$9.699\cdot10^{8}$	5.0	$4.8\cdot10^{7}$
	125m ($t_{1/2}$ = 9.52 min)	$9.911\cdot10^{9}$	5.0	$5.0\cdot10^{8}$
	125	$1.157\cdot10^{10}$	4.9	$5.7\cdot10^{8}$
	126	$5.076\cdot10^{10}$	5.0	$2.5\cdot10^{9}$
	127m ($t_{1/2}$ = 4.13 min)	$1.195\cdot10^{10}$	5.0	$6.0\cdot10^{8}$
	127	$9.591\cdot10^{10}$	4.8	$4.6\cdot10^{9}$
	128	$3.047\cdot10^{11}$	2.4	$7.4\cdot10^{9}$
	129m ($t_{1/2}$ = 6.9 min)	$1.821\cdot10^{11}$	5.0	$9.1\cdot10^{9}$
	129	$2.510\cdot10^{11}$	4.6	$1.2\cdot10^{10}$
	130	$1.027\cdot10^{12}$	5.0	$5.1\cdot10^{10}$
	131	$8.622\cdot10^{11}$	4.4	$3.8\cdot10^{10}$
	132	$5.717\cdot10^{11}$	4.2	$2.4\cdot10^{10}$
	133	$1.413\cdot10^{11}$	0.9	$1.2\cdot10^{9}$
	134	$2.067\cdot10^{10}$	0.7	$1.5\cdot10^{8}$
	135	$1.113\cdot10^{9}$	0.3	$3.7\cdot10^{6}$
	136	$5.580\cdot10^{7}$	0.2	$8.4\cdot10^{4}$
	137	$1.782\cdot10^{7}$	0.1	$1.9\cdot10^{4}$
	138	$1.169\cdot10^{5}$	0.05	$5.3\cdot10^{1}$

Table 7: Calculated intensities of several secondary beams in case of natural uranium target. Efficiency values given in column 4 comprise release, ionisation and beam-preparation efficiencies.

Element	**Mass number**	**In-target rate (at/s)**	**Efficiency (%)**	**Intensity (ions/s)**
Nickel (Z=28)	66	$2.3179\cdot10^{5}$	< 63.8	$< 1.5\cdot10^{5}$
	67	$1.1013\cdot10^{6}$	< 14.2	$< 1.6\cdot10^{5}$
	68	$4.2876\cdot10^{6}$	< 17.4	$< 7.4\cdot10^{5}$
	69	$9.9061\cdot10^{6}$	7.7	$< 7.6\cdot10^{5}$
	70	$1.8365\cdot10^{7}$	4.0	$7.4\cdot10^{5}$
	71	$2.4715\cdot10^{7}$	1.5	$3.8\cdot10^{5}$
	72	$2.4881\cdot10^{7}$	0.8	$2.0\cdot10^{5}$
	73	$2.0777\cdot10^{7}$	0.35	$7.2\cdot10^{4}$
	74	$9.8522\cdot10^{6}$	0.35	$3.5\cdot10^{4}$
	75	$3.7725\cdot10^{6}$	0.083	$3.1\cdot10^{3}$
	76	$9.6381\cdot10^{5}$	0.047	$4.5\cdot10^{2}$
	77	$1.4716\cdot10^{5}$	0.037	$5.5\cdot10^{1}$
	78	$2.0046\cdot10^{4}$	0.032	6.3

	80	$9.3817\cdot10^{1}$	0.008	0.8
Gallium (Z=31)	68	1.856	5.0	$9.3\cdot10^{-2}$
	69	$6.342\cdot10^{1}$	5.0	3.2
	70	$1.554\cdot10^{3}$	5.0	$7.8\cdot10^{1}$
	71	$2.828\cdot10^{4}$	5.0	$1.4\cdot10^{3}$
	72	$3.088\cdot10^{5}$	5.0	$1.5\cdot10^{4}$
	73	$3.575\cdot10^{6}$	5.0	$1.8\cdot10^{5}$
	74	$2.201\cdot10^{7}$	5.0	$1.1\cdot10^{6}$
	75	$1.273\cdot10^{8}$	4.9	$6.3\cdot10^{6}$
	76	$5.009\cdot10^{8}$	4.9	$2.4\cdot10^{7}$
	77	$1.483\cdot10^{9}$	4.5	$6.7\cdot10^{7}$
	78	$3.436\cdot10^{9}$	4.0	$1.4\cdot10^{8}$
	79	$6.031\cdot10^{9}$	3.5	$2.1\cdot10^{8}$
	80	$4.565\cdot10^{9}$	3.0	$1.4\cdot10^{8}$
	81	$3.164\cdot10^{9}$	2.6	$8.3\cdot10^{7}$
	82	$1.968\cdot10^{9}$	1.8	$3.5\cdot10^{7}$
	83	$2.475\cdot10^{8}$	1.1	$2.7\cdot10^{6}$
	84	$2.328\cdot10^{9}$	0.3	$7.8\cdot10^{6}$
	85	$4.470\cdot10^{6}$	0.2	$8.4\cdot10^{3}$
	86	$7.038\cdot10^{6}$	0.1	$7.3\cdot10^{3}$
Krypton (Z=36)	83m ($t_{1/2}$ = 1.83 h)	$3.9654\cdot10^{5}$	8.8	$3.5\cdot10^{4}$
	85m ($t_{1/2}$ = 4.48 h)	$1.2303\cdot10^{9}$	8.8	$1.1\cdot10^{8}$
	85	$5.3806\cdot10^{9}$	8.8	$4.7\cdot10^{8}$
	87	$1.0022\cdot10^{11}$	9.2	$9.2\cdot10^{9}$
	88	$3.8758\cdot10^{11}$	8.8	$3.4\cdot10^{10}$
	89	$7.7351\cdot10^{11}$	8.5	$6.6\cdot10^{10}$
	90	$1.0254\cdot10^{12}$	8.4	$8.7\cdot10^{10}$
	91	$7.9198\cdot10^{11}$	7.0	$5.5\cdot10^{10}$
	92	$4.5862\cdot10^{11}$	4.9	$2.3\cdot10^{10}$
	93	$1.5948\cdot10^{11}$	4.4	$7.0\cdot10^{9}$
	94	$4.6897\cdot10^{10}$	1.3	$6.3\cdot10^{8}$
	95	$7.0155\cdot10^{9}$	0.7	$4.7\cdot10^{7}$
	96	$9.1159\cdot10^{9}$	0.6	$5.8\cdot10^{7}$
	97	$7.4091\cdot10^{7}$	0.5	$3.9\cdot10^{5}$
	98	$3.4620\cdot10^{8}$	0.4	$1.3\cdot10^{6}$
	100	$2.5367\cdot10^{5}$	0.2	$6.1\cdot10^{2}$
Tin (Z=50)	118	$2.668\cdot10^{3}$	5.0	$1.3\cdot10^{2}$

	119	$4.854\cdot10^{4}$	5.0	$2.4\cdot10^{3}$
	121m ($t_{1/2}$ = 55 y)	$9.119\cdot10^{6}$	5.0	$4.6\cdot10^{5}$
	121	$7.454\cdot10^{7}$	5.0	$3.7\cdot10^{6}$
	123m ($t_{1/2}$ = 40.06 min)	$1.077\cdot10^{8}$	5.0	$5.4\cdot10^{6}$
	123	$3.533\cdot10^{8}$	5.0	$1.8\cdot10^{7}$
	125m ($t_{1/2}$ = 9.52 min)	$2.971\cdot10^{9}$	5.0	$1.5\cdot10^{8}$
	125	$5.348\cdot10^{9}$	4.9	$2.6\cdot10^{8}$
	126	$2.051\cdot10^{10}$	5.0	$1.0\cdot10^{9}$
	127m ($t_{1/2}$ = 4.13 min)	$6.054\cdot10^{9}$	5.0	$3.0\cdot10^{8}$
	127	$3.736\cdot10^{10}$	4.8	$1.8\cdot10^{9}$
	128	$1.049\cdot10^{11}$	2.4	$2.5\cdot10^{9}$
	129m ($t_{1/2}$ = 6.9 min)	$5.338\cdot10^{10}$	5.0	$2.7\cdot10^{9}$
	129	$9.640\cdot10^{10}$	4.6	$4.5\cdot10^{9}$
	130	$3.164\cdot10^{11}$	5.0	$1.6\cdot10^{10}$
	131	$2.799\cdot10^{11}$	4.4	$1.2\cdot10^{10}$
	132	$1.865\cdot10^{11}$	4.2	$7.8\cdot10^{9}$
	133	$5.103\cdot10^{10}$	0.9	$4.4\cdot10^{8}$
	134	$9.133\cdot10^{9}$	0.7	$6.6\cdot10^{7}$
	135	$6.991\cdot10^{8}$	0.3	$2.3\cdot10^{6}$
	136	$4.591\cdot10^{7}$	0.2	$6.9\cdot10^{4}$
	137	$5.811\cdot10^{6}$	0.1	$6.2\cdot10^{3}$
	138	$1.165\cdot10^{5}$	0.05	$5.3\cdot10^{1}$

Table 8: Calculated intensities of several secondary beams in case of depleted uranium target. Efficiency values given in column 4 comprise release, ionisation and beam-preparation efficiencies.

Element	**Mass number**	**In-target rate (at/s)**	**Efficiency (%)**	**Intensity (ions/s)**
Nickel (Z=28)	66	$2.2450\cdot10^{5}$	< 63.8	$< 1.4\cdot10^{5}$
	67	$1.0546\cdot10^{6}$	< 14.2	$< 1.5\cdot10^{5}$
	68	$4.1419\cdot10^{6}$	< 17.4	$< 7.2\cdot10^{5}$
	69	$9.5772\cdot10^{6}$	7.7	$7.3\cdot10^{5}$
	70	$1.7659\cdot10^{7}$	4.0	$7.1\cdot10^{5}$
	71	$2.3699\cdot10^{7}$	1.5	$3.6\cdot10^{5}$
	72	$2.3377\cdot10^{7}$	0.8	$1.9\cdot10^{5}$
	73	$1.9424\cdot10^{7}$	0.35	$6.8\cdot10^{4}$
	74	$9.0368\cdot10^{6}$	0.35	$3.2\cdot10^{4}$
	75	$3.4999\cdot10^{6}$	0.083	$2.9\cdot10^{3}$

	76	$8.7445\cdot10^{5}$	0.047	$4.1\cdot10^{2}$
	77	$1.3698\cdot10^{5}$	0.037	$5.1\cdot10^{1}$
	78	$1.9175\cdot10^{4}$	0.032	6.0
	80	$9.3428\cdot10^{1}$	0.008	0.7
Gallium (Z=31)	68	1.696	5.0	$8.5\cdot10^{-2}$
	69	$5.943\cdot10^{1}$	5.0	3.0
	70	$1.467\cdot10^{3}$	5.0	$7.3\cdot10^{1}$
	71	$2.695\cdot10^{4}$	5.0	$1.3\cdot10^{3}$
	72	$2.919\cdot10^{5}$	5.0	$1.\ 5\cdot10^{4}$
	73	$3.297\cdot10^{6}$	5.0	$1.6\cdot10^{5}$
	74	$1.935\cdot10^{7}$	5.0	$9.7\cdot10^{5}$
	75	$9.606\cdot10^{7}$	4.9	$4.7\cdot10^{6}$
	76	$3.308\cdot10^{8}$	4.9	$1.6\cdot10^{7}$
	77	$8.325\cdot10^{8}$	4.5	$3.8\cdot10^{7}$
	78	$1.838\cdot10^{9}$	4.0	$7.4\cdot10^{7}$
	79	$3.412\cdot10^{9}$	3.5	$1.2\cdot10^{8}$
	80	$2.776\cdot10^{9}$	3.0	$8.3\cdot10^{7}$
	81	$1.926\cdot10^{9}$	2.6	$5.1\cdot10^{7}$
	82	$1.032\cdot10^{9}$	1.8	$1.8\cdot10^{7}$
	83	$2.181\cdot10^{8}$	1.1	$2.4\cdot10^{6}$
	84	$6.778\cdot10^{8}$	0.3	$2.\ 3\cdot10^{6}$
	85	$4.386\cdot10^{6}$	0.2	$8.2\cdot10^{3}$
	86	$2.161\cdot10^{6}$	0.1	$2.3\cdot10^{3}$
Krypton (Z=36)	83m ($t_{1/2}$ = 1.83 h)	$1.5519\cdot10^{5}$	8.8	$1.4\cdot10^{4}$
	85m ($t_{1/2}$ = 4.48 h)	$3.5226\cdot10^{8}$	8.8	$3.1\cdot10^{7}$
	85	$1.5753\cdot10^{9}$	8.8	$1.4\cdot10^{8}$
	87	$3.0416\cdot10^{10}$	9.2	$2.8\cdot10^{9}$
	88	$1.2729\cdot10^{11}$	8.8	$1.1\cdot10^{10}$
	89	$2.5586\cdot10^{11}$	8.5	$2.2\cdot10^{10}$
	90	$3.6187\cdot10^{11}$	8.4	$3.1\cdot10^{10}$
	91	$3.1562\cdot10^{11}$	7.0	$2.2\cdot10^{10}$
	92	$2.0894\cdot10^{11}$	4.9	$1.0\cdot10^{10}$
	93	$8.6684\cdot10^{10}$	4.4	$3.8\cdot10^{9}$
	94	$3.3933\cdot10^{10}$	1.3	$4.5\cdot10^{8}$
	95	$5.9123\cdot10^{9}$	0.7	$3.9\cdot10^{7}$
	96	$3.4942\cdot10^{9}$	0.6	$2.2\cdot10^{7}$
	97	$6.9633\cdot10^{7}$	0.5	$3.6\cdot10^{5}$

	98	$1.0382\cdot10^{8}$	0.4	$3.9\cdot10^{5}$
	100	$8.2705\cdot10^{4}$	0.2	$2.0\cdot10^{2}$
Tin (*Z*=50)	118	$1.171\cdot10^{3}$	5.0	$5.9\cdot10^{1}$
	119	$2.103\cdot10^{4}$	5.0	$1.1\cdot10^{3}$
	121m ($t_{1/2}$ = 55 y)	$4.190\cdot10^{6}$	5.0	$2.1\cdot10^{5}$
	121	$2.111\cdot10^{7}$	5.0	$1.1\cdot10^{6}$
	123m ($t_{1/2}$ = 40.06 min)	$5.561\cdot10^{7}$	5.0	$2.8\cdot10^{6}$
	123	$2.116\cdot10^{8}$	5.0	$1.1\cdot10^{7}$
	125m ($t_{1/2}$ = 9.52 min)	$1.375\cdot10^{9}$	5.0	$6.9\cdot10^{7}$
	125	$3.916\cdot10^{9}$	4.9	$1.9\cdot10^{8}$
	126	$1.355\cdot10^{10}$	5.0	$6.8\cdot10^{8}$
	127m ($t_{1/2}$ = 4.13 min)	$4.697\cdot10^{9}$	5.0	$2.3\cdot10^{8}$
	127	$2.389\cdot10^{10}$	4.8	$1.1\cdot10^{9}$
	128	$5.893\cdot10^{10}$	2.4	$1.4\cdot10^{9}$
	129m ($t_{1/2}$ = 6.9 min)	$2.379\cdot10^{10}$	5.0	$1.2\cdot10^{9}$
	129	$6.084\cdot10^{10}$	4.6	$2.8\cdot10^{9}$
	130	$1.530\cdot10^{11}$	5.0	$7.7\cdot10^{9}$
	131	$1.460\cdot10^{11}$	4.4	$6.4\cdot10^{9}$
	132	$9.797\cdot10^{10}$	4.2	$4.1\cdot10^{9}$
	133	$3.027\cdot10^{10}$	0.9	$2.6\cdot10^{8}$
	134	$6.482\cdot10^{9}$	0.7	$4.7\cdot10^{7}$
	135	$6.042\cdot10^{8}$	0.3	$2.0\cdot10^{6}$
	136	$4.364\cdot10^{7}$	0.2	$6.5\cdot10^{4}$
	137	$3.051\cdot10^{6}$	0.1	$3.2\cdot10^{3}$
	138	$1.164\cdot10^{5}$	0.05	$5.3\cdot10^{1}$

3.4. Two-step option

In Table 9 are given expected yields of several nuclei in two-step option, using a post-accelerated ^{132}Sn beam. The method is described in Section 2.2.2.

The strength of the two-step method is clearly seen if we compare the intensities given in Table 9 with those obtained at ISOLDE. At present, at ISOLDE maximum available intensities of ^{131}In and ^{130}Cd beams are $5\cdot10^{5}$ ions/μC and $1\cdot10^{4}$ ions/μC, respectively. If one assume 100 μA proton beam (as it will be available at EURIOSL), one could make an estimate of $5\cdot10^{7}$ ions/s and $1\cdot10^{6}$ ions/s for, respectively, ^{131}In and ^{130}Cd beams in a direct target configuration. By comparing these numbers with those given in Table 9, one can see that the two-step option gives an enhancement in intensities of these two beams of about factor of 100.

Table 9: Secondary-beam intensity in the two-step option assuming re-accelerated ^{132}Sn beam at 150·A MeV and intensity of 10^{13} part/s impinging on 500 mg/cm^2 thick Be target.

Element	Mass number	Intensity (ions/s)
Indium (*Z*=49)	131	$8.5\cdot10^{9}$
Cadmium (*Z*=48)	130	$1.1\cdot10^{8}$
Silver (*Z*=47)	129	$1.6\cdot10^{6}$
Palladium (*Z*=46)	128	$2.3\cdot10^{4}$
Rhodium (*Z*=45)*	127	153
Ruthenium (*Z*=44)*	126	1.4
	125	13.8
	124	414
Technetium (*Z*=43)*	123	4.3
	122	24.6
	121	281
Molybdenum (*Z*=42)*	120	5
	119	18
	118	171
	117	481
	116	$2.8\cdot10^{3}$
	115	$6.8\cdot10^{3}$
	114	$2.9\cdot10^{4}$
Niobium (*Z*=41)*	117	3
	116	11
	115	79
	114	240
	113	$1.2\cdot10^{3}$
	112	$3.3\cdot10^{3}$
	111	$1.3\cdot10^{4}$
Zirconium (*Z*=40)*	114	2
	113	5
	112	40
	111	113
	110	625
	109	$1.6\cdot10^{3}$

** Refractory elements*

4. Conclusions

As a summary, in Figure 23 are presented intensities of some of the nuclides considered in the present report. For those nuclei, which are produced using different options/targets, a maximum calculated intensity is given.

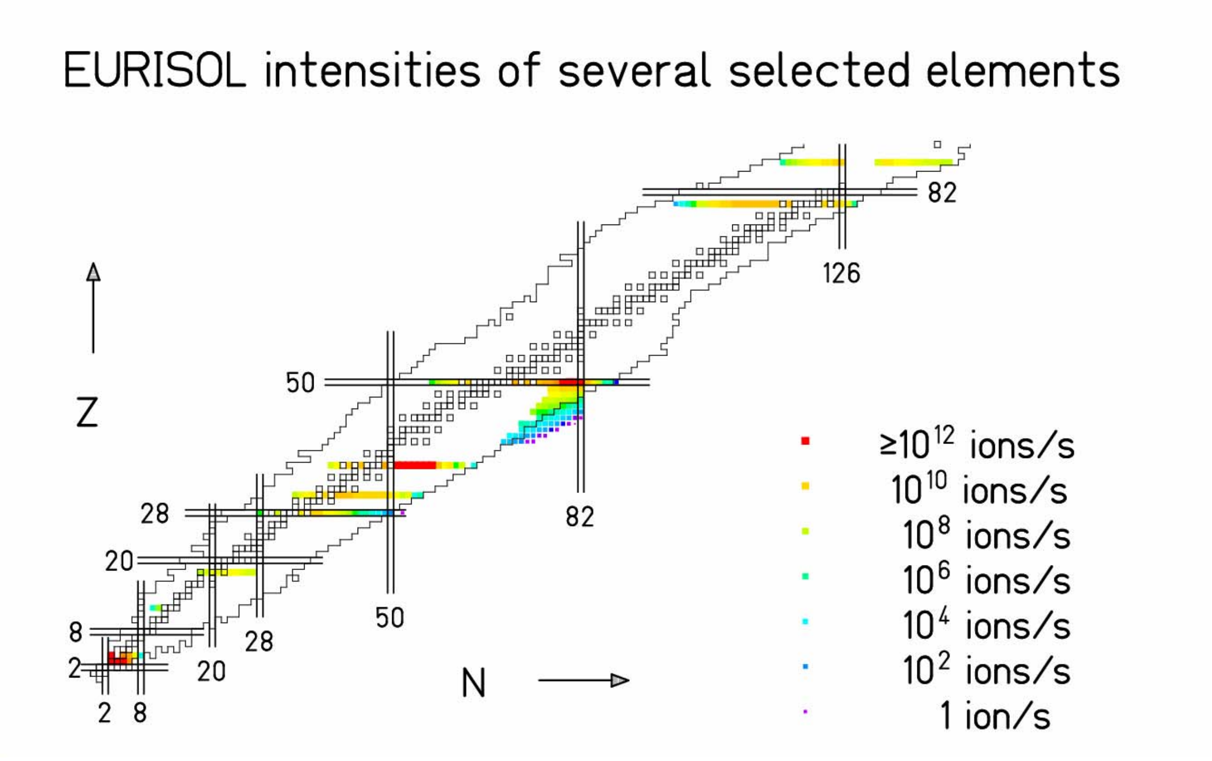

Figure 23: Expected EURISOL intensities of several selected nuclei presented on the chart of nuclides. Numerical values are given in Section 3.

References:

---

[1] http://www.eurisol.org/site02/index.php
[2] http://pro.ganil-spiral2.eu/eurisol/feasibility-study-reports/feasibility-study-appendix-c
[3] http://www.gsi.de/charms/Publications/publica.htm
[4] http://www.eurisol.org/site02/direct_target/
[5] http://www.eurisol.org/site02/fission_target/
[6] http://www.eurisol.org/site02/beam_preparation/
[7] K. Helariutta et al., Eur. Phys. J. A17 (2003) 181
[8] C. Villagrasa-Canton et al., Phys. Rev. C 75 (2007) 044603
[9] P. Napolitani et al., Phys. Rev. C 70 (2004) 054607
[10] P. Napolitani et al., Phys. Rev. C 76 (2007) 064609
[11] T. Enqvist et al., Nucl. Phys. A 686 (2001) 481
[12] J. Taieb et al., Nucl. Phys. A 724 (2003) 413
[13] M. Bernas et al., Nucl. Phys. A 725 (2003) 213
[14] M. V. Ricciardi et al., Phys. Rev. C 73 (2006) 014607
[15] P. Armbruster et al., Phys. Rev. Lett. 93 (2004) 212701
[16] J. Benlliure et al, Nucl. Phys. A660 (1999) 87
[17] J.-J. Gaimard and K.-H. Schmidt, Nucl. Phys. A 531 (1991) 709
[18] A. Kelić, M.V. Ricciardi and K.-H. Schmidt, arXiv_nucl-th/0906.4193v1; Proceedings of Joint ICTP-IAEA Advanced Workshop on Model Codes for Spallation Reactions, ICTP Trieste, Italy, 4-8 February 2008. Editors: D. Filges, S. Leray, Y. Yariv, A. Mengoni, A. Stanculescu, and G. Mank, IAEA INDC(NDS)-530, p. 181-221, Vienna, August 2008

---

[19] EURISOL_DS Task 11, Deliverable D4 (11-25-2009-0015), available at: http://www.eurisol.org/site02/beam_intensity_calculations/

[20] R.J. Glauber, Proceeding of the conference High-Energy Physics and Nuclear Structure, New York 1970, 207-264.

[21] D. Henzlova et al., Phys. Rev. C 78 (2008) 044616

[22] A. Kelić et al., Phys. Rev. C 70 (2004) 064608,

[23] K. Sümmerer and B. Blank, Phys. Rev. C61 (2000) 034607

[24] M. Caamaño, et al. Nucl. Phys. A 733 (2004) 187

[25] R.E. Tribble, R.H. Burch and C.A. Gagliardi, Nucl. Instr. and Meth. A285 (1989) 441; R.E. Tribble, C.A. Gagliardi and W. Liu, Nucl. Instr. and Meth. B56/57 (1991) 956.

[26] M. Veselsky and G.A. Souliotis, Report on „Production of exotic nuclides in nucleus-nucleus collisions in the Fermi-energy domain“ (11-25-2009-0018), available at: http://www.eurisol.org/site02/beam_intensity_calculations/

[27] G.A. Souliotis et al., Phys. Rev. Lett. 91 (2003) 022701

[28] H. Penttilä et al, Eur. Phys. J. Special Topics 150 (2007) 317

[29] V. Kolhinen, T. Eronen, U. Hager, J. Hakala, A. Jokinen, S. Kopecky, S. Rinta-Antila, J. Szerypo and J. Äystö, Nucl. Instr. and Meth. A **528** (2004) 776

[30] H. Penttilä et al, Proceedings of the Fourth International Conference Fission and Properties of Neutron-Rich Nuclei, Sanibel Island, Florida, November 11-17, 2007, p. 410, ed. J.H. Hamilton, A.V.Ramayya, H.K.Carter, World Scientific, Singapore, 2008

[31] EURISOL_DS Task 11, Deliverable D5 (11-25-2008-0021), available at: http://www.eurisol.org/site02/beam_intensity_calculations/

[32] V.A. Rubchenya, Phys. Rev. C75 (2007) 054601

[33] B. Jurado et al., Nucl. Phys. A 747 (2005) 14

[34] C. Schmitt et al., Phys. Rev. Lett. 99 (2007) 042701

[35] J. Benlliure et al., Nucl. Phys. A628 (1998) 458

[36] K. Kruglov et al., Eur. Phys. J. A 14 (2002) 365

[37] A. Kelić, M. V. Ricciardi and K.-H. Schmidt, in Proceedings of the International Conference on Nuclear Data for Science and Technology, April 22-27, 2007, Nice, France, editors O. Bersillon, F. Gunsing, E. Bauge, R. Jacqmin, and S. Leray, EDP Sciences, 2008, Volume 2, ISBN: 978-2-7598-0091-9, pp 1113-1116.

[38] K.-H. Schmidt, A. Kelić, M. V. Ricciardi, Europhys. Lett. 83 (2008) 32001

[39] F. Vives et al., Nucl. Phys. A 662 (2000) 63

[40] C. M. Zöller, PhD thesis, Technical University Darmstadt, 1995

[41] K.-H. Schmidt et al., Nucl. Phys. A 665 (2000) 221

[42] U. Köster, Radiochim. Acta 89 (2001) 749

[43] http://isolde.web.cern.ch/ISOLDE/normal/isoprodsc.html

[44] K.-H. Schmidt et al., Phys. Rev. ST Accel. Beams 10 (2007) 014701

[45] A. Boudard, J. Cugnon, S. Leray, and C. Volant, Phys. Rev. C 66 (2002) 044615

[46] EURISOL_DS Task 11, Deliverable D2 (11-25-2009-0023), available at: http://www.eurisol.org/site02/beam_intensity_calculations/

[47] EURISOL_DS Task 11, Milestone M6.1 (11-25-2007-0003, 11-25-2007-0006, 11-25-2007-0008), available at: http://www.eurisol.org/site02/beam_intensity_calculations/

[48] S. Chabod et al., „In-target radioactive nuclei production rates with EURISOL single-stage target configuration“, EURISOL_DS Task 11, report: 11-25-2009-0022, , available at: http://www.eurisol.org/site02/beam_intensity_calculations/; S. Chabod et al, „Optimization of in-target yields for RIB production: Par I: direct targets“, EURISOL_DS Task 11, report 11-25-2008-0011

[49] The EURISOL report, Feasibility study for the EURopean Isotope-Separation-On-Line radioactive beam facility (appendix C) (2003), available at: www.ganil.fr/eurisol/Final_Report.html

[50] R.D. Page *et al.*, Selection of key experiments with the associated instrumentation, available at: www.eurisol.org/site02/doc_details.php?EURpub=1&dID=725&tID=14

[51] D. Ene et al., „In-target yields for RIB production: Part II: two-stage target configuration“, EURISOL_DS Task 11, report 11-25-2009-0022, available at: http://www.eurisol.org/site02/beam_intensity_calculations/

---

[52] S. Lukić et al., Nucl. Instrum. Meth. A 565 (2006) 784

[53] A. E. Barzakh et al, „Report on the R&D of Uranium Carbide targets by the PLOG collaboration at PNPI-Gatchina“, EURISOL_DS Task 4, report 04-25-2007-0005, available at: http://www.eurisol.org/site02/fission_target/publications_internal_task_note.php?tID=&type=25

[54] D. Lunney et al., „Advanced low-energy beam transport, mass purification and facility“, EURISOL_DS Task 9, Deliverable D7 (09-25-2009-0007), available at: http://www.eurisol.org/site02/beam_preparation/

[55] P. Delahaye et al., „Advance in charge-breading research and developments“, EURISOL_DS Task 9, Deliverable D7 (09-25-2009-0010), available at: http://www.eurisol.org/site02/beam_preparation/

[56] J.R.J. Bennett et al., Nucl. Instr. Meth. B204 (2003) 215

[57] Thierry Stora, *private communication*

[58] S. Fernandes et al., „Diffusion studies in prospective polycrystalline silicon carbide target materials for radioactive ion beam production at CERN-ISOLDE“, EURISOL_DS Task 3, report 03-25-2008-0010, available at: http://www.eurisol.org/site02/direct_target/